

Optics technology for large-aperture space telescopes: from fabrication to final acceptance tests

ISAAC TRUMPER,¹ PASCAL HALLIBERT,² JONATHAN W. ARENBERG,³
HIDEYO KUNIEDA,⁴ OLIVIER GUYON,^{5,6}  H. PHILIP STAHL,⁷ AND
DAE WOOK KIM^{1,5,*}

¹College of Optical Sciences, University of Arizona, 1630 E. University Blvd., Tucson, Arizona 85721, USA

²European Space Agency (ESA), ESTEC Keplerlaan 1, 2200 AG Noordwijk, The Netherlands

³Northrop Grumman Aerospace Systems, One Space Park Drive, Redondo Beach, California 90278, USA

⁴Department of Physics, School of Science, Nagoya University, Furo-cho, Chikusa-ku, Nagoya, Aichi 464-8602, Japan

⁵Department of Astronomy and Steward Observatory, University of Arizona, 933 N. Cherry Ave., Tucson, Arizona 85719, USA

⁶Subaru Telescope, National Observatory of Japan, Hilo, Hawaii 96720, USA

⁷NASA Marshall Space Flight Center, Huntsville, Alabama 35812, USA

*Corresponding author: letter2dwk@hotmail.com

Received March 19, 2018; revised July 11, 2018; accepted July 12, 2018; published August 28, 2018 (Doc. ID 315379)

This review paper addresses topics of fabrication, testing, alignment, and as-built performance of reflective space optics for the next generation of telescopes across the x-ray to far-infrared spectrum. The technology presented in the manuscript represents the most promising methods to enable a next level of astronomical observation capabilities for space-based telescopes as motivated by the science community. While the technology to produce the proposed telescopes does not exist in its final form, the optics industry is making steady and impressive progress toward these goals across all disciplines. We hope that through sharing these developments in context of the science objectives, further connections and improvements are enabled to push the envelope of the technology. © 2018 Optical Society of America

OCIS codes: (350.6090) Space optics; (350.1260) Astronomical optics; (230.4040) Mirrors; (120.3940) Metrology; (120.4610) Optical fabrication; (220.1140) Alignment

<https://doi.org/10.1364/AOP.10.000644>

1. Introduction	646
1.1. Review Methodology	646
2. Technology Requirements for Science Objectives	647
2.1. X-Ray Science	647
2.2. UV/Optical/IR Science	651

2.3. Mid- to Far-Infrared Science	654
2.4. Synopsis of Science Drivers	657
3. Large Light-Weighted Mirror Fabrication	657
3.1. Producing a Stiff, Light, and Low Expansion Mirror Substrate	657
3.1a. X-Ray Optics Substrates	658
3.1b. UVOIR Mirror Substrates	659
3.1c. Mid- to Far-Infrared Optics Substrates	660
3.2. Grinding, Polishing, and Figuring Processes	661
3.2a. Primary Mirror Surfaces	662
3.2b. Secondary Mirror Surfaces	665
4. Testing In-Process Optical Surfaces	666
4.1. Full-Spectrum Metrology Requirements for Astronomical Telescopes	666
4.2. Rough Generation Stage: Measuring and Controlling the Global Shape	666
4.3. Polishing and Figuring Stage: Measuring and Perfecting the Surface Quality	668
4.4. Final Verification of Space Optics	671
4.4a. Null Testing of Concave Optics	671
4.4b. Null Testing of Convex Optics	671
4.4c. As-Flown Characterization	672
4.5. Optical Coating	675
5. Component and Instrument Alignment of Optical and Mechanical Systems	675
5.1. Optical System Alignment	676
5.2. Segmented Mirror Alignment	678
6. Optical System Performance: End-to-End Testing	679
6.1. Telescope Testing	679
6.2. Active Correction	681
6.3. Stray Light Suppression	684
7. Concluding Remarks	684
Acknowledgment	685
References	685

Optics technology for large-aperture space telescopes: from fabrication to final acceptance tests

ISAAC TRUMPER, PASCAL HALLIBERT, JONATHAN W. ARENBERG, HIDEYO KUNIEDA, OLIVIER GUYON, H. PHILIP STAHL, AND DAE WOOK KIM

1. INTRODUCTION

Space optical systems are key to furthering our fundamental understanding of the universe in which we live. They provide measurements of phenomenon across space and time, allowing us to probe the most exciting astrophysics questions of our time through the electromagnetic spectrum. Optical measurements have identified planets orbiting distant stars, many of which reside in the habitable zone (HZ) of their parent star. The age, size, and shape of the universe are examined with space optics, which allows us to draw conclusions about the past and future trajectory of its existence. In the National Academy 2010 Decadal Report, *New Worlds, New Horizons* [1], the National Research Council (NRC) identified three priority science objectives for the coming decade: Cosmic Dawn: searching for the first stars, galaxies, and black holes; New Worlds: seeking nearby, habitable planets; and Physics of the Universe: understanding scientific principles. The European Space Agency (ESA) has defined five topics of interest for future space missions: the hot and energetic universe, planets and life, the solar system, fundamental laws, and the Universe [2]. In 2020 the National Academy is expected to review four potential missions (Habitable Exoplanet Imaging Mission [3], Large Ultraviolet/Optical/Infrared Surveyor (LUVOIR) [4], Origins Space Telescope [5], and Lynx X-ray Surveyor [6]), and recommend the National Aeronautics and Space Administration's (NASA) next large mission to advance our knowledge and understanding of NASA's most compelling science questions. As discussed in this review paper, all of these potential missions require significant advances in telescope fabrication and acceptance test technology. Realizing the optical elements to enable these missions will require advances in space optics technology across all aspects of the field. This review paper of current space optics technology serves as a reference to the status of each critical technology such that future work in these areas can benefit from the previous work of other researchers. We hope to provide a succinct and comprehensive overview of technologies we believe to be at the forefront of their field and those that are poised to enable the next generation of space optical telescopes.

1.1. Review Methodology

In this review paper, the technologies for the future large-aperture space telescopes are separated into four core areas: fabrication, testing, alignment, and as-built performance. In each section, key technologies that have been developed to move the scientific community closer to the science objectives outlined above will be highlighted. The results from the published works will be put in the context of the role they serve to meet the specifications required to enable the next generation of space optics. Within each sub-section, we have further differentiated the various technologies by the wavelength regime of the telescope, breaking the electromagnetic spectrum into three main

categories: x-ray, UVOIR, and mid- to far-infrared (MFIR). We define the energy/wavelength range of each category as: x-rays from 0.3 to 100 keV, UVOIR to range from 100 nm to 2 μm , and MFIR from 2 to 500 μm . Note that the boundaries are flexible depending on the exact mission specifications, but this serves as a general definition for terminology throughout the review. We attempt to provide a forward looking review of these key technologies and hope that readers will apply the knowledge presented here to improve existing methods, innovate, and further our understanding of optics technology for large-aperture space telescopes. In this review, we prioritized the key technologies at the forefront of their respective fields that will enable the next generation of space-based large-aperture reflective telescopes over older methods.

2. TECHNOLOGY REQUIREMENTS FOR SCIENCE OBJECTIVES

Based on the mission objectives and science goals of each scientific area of interest, as identified by the NRC [1] or ESA [2], the engineering specifications for the next generation of space optical systems have been proposed and discussed in the literature. These specifications serve as a goal for the development of space optics technologies to enable the optics that will be used in the various telescopes. When the optics can be manufactured to the standards determined by the science and at a cost that is affordable, the next generation of space telescopes will launch. The top-level flow down of specifications comes from determining the highest priority science goals for the future, analyzing the measurements and data required to make scientific conclusions about these topics, and then choosing the correct optical specification that will ensure the data meets the quality standards. The next step translates the performance metrics of the science into engineering specifications for the production of the optics, which sets the requirements for the technology used during the manufacturing process. Understanding this relationship between the science objectives and the technology requirements is critical to ensure that the tools used in fabrication, testing, alignment, and performance testing are developed in a holistic manner and are well justified.

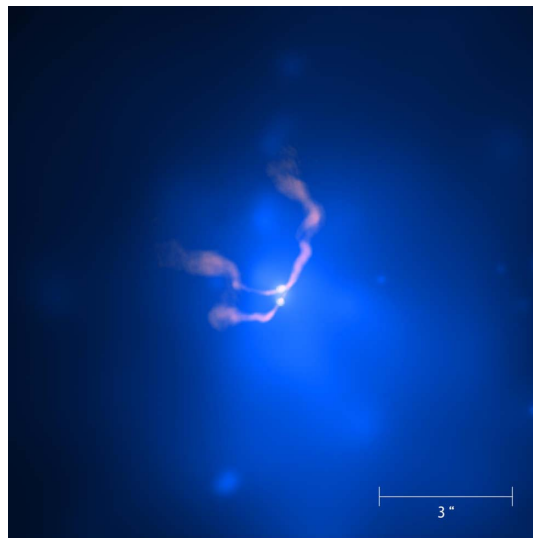
2.1. X-Ray Science

The next generation of x-ray telescopes will provide more than an order of magnitude improvement in performance compared to the current telescopes, namely *Chandra* and *XMM-Newton*, in areas of imaging, spectroscopy, timing, and polarimetry [7]. The *International X-ray Observatory (IXO)* was a joint Japan Aerospace Exploration Agency (JAXA)/NASA/ESA mission designed to address major astrophysics questions, concerning the formation and characterization of black holes, life cycles of matter, and energy in the cosmos [1,8]. Upon review by the ESA in 2011, the IXO mission was revised to be an ESA-led program under the name *Advanced Telescope for High ENergy Astrophysics (ATHENA)* [9] with the goals of studying the hot and energetic universe by mapping the hot gas structures, determining their physical properties, and searching for supermassive black holes (SMBHs) [2]. By mapping gas found in the intergalactic medium as well as clusters and groups of galaxies, the data from x-ray science will determine the physical properties and dynamics of these structures by tracking their evolution through cosmic time. This data will allow us to answer questions such as “How does ordinary matter assemble into the large-scale structures we see today? What happens at the very edge of a black hole? How do black holes grow and shape the Universe? What is the equation of state of matter at supranuclear density?” Results from these future experiments will produce data that shows the beauty of our Universe, as exemplified by the merging of two galaxies shown in Fig. 1.

To probe these topics, x-ray telescopes with very large collection areas and high angular resolution are required to image the extreme energetics of the interactions close to the event horizon of black holes. Shown in Table 1 is a summary of the driving specifications for the next generation of x-ray telescopes. The search for the first supermassive black hole drives the requirement on sensitivity [7], which relies on detecting a significant number of low-luminosity (distant and faint) active galactic nuclei (AGN) at redshifts of $z = 6-10$. The luminosity of the AGN in the rest frame (2–10 keV) is typically 10^{43} erg s⁻¹, which creates the point source detection sensitivity specification of $\sim 10^{-17}$ erg cm⁻² s⁻¹ in the observed frame (0.5–2 keV) [19]. Characterizing the supermassive black hole growth in the early Universe drives the x-ray telescope effective area, angular resolution, and wide field imaging requirements. A 5 arcsec beam is the limit of the angular resolution to achieve the desired sensitivity due to the fluctuation of the x-ray background flux in the beam [20].

Intrinsically tied to the angular resolution and sensitivity specifications is the requirement on the effective collection area of the next x-ray telescope, which is driven by peak fluxes around 1–2 keV and photon-limited science. To obtain the required angular resolution and sensitivity within the time constraints of a typical observatory program of 8 month surveys, an effective area of at least 2.5 m² is required in the 1–2 keV regime to detect sufficient numbers of individual distant and faint AGN with the fluxes described above. While at 6 keV, an effective area of 0.65 m² will ensure >100 photons in the iron (Fe) line from a supermassive black hole during one orbital period of the inner most annulus of the accretion disk to reveal the relativistic modulation of the line profile. At the higher energies of 30 keV, where an accurate determination of the continuum under the Fe line is needed, an effective area of 350 cm² is

Figure 1



Rare example of two galaxies caught in the act of merging, emitting x-rays (blue) and radio waves (pink). As their central black holes merge, they each produce radio jets surrounded by an enormous cloud of multimillion degree gas emitting x-rays. By analyzing these two data, the direction and motion of the two black holes was determined. The swept-back appearance of the jets is due to the rapid motion of the galaxies. Source: x-ray: NASA/CXC/AIfA/D.Hudson [10]; Radio: NRAO/CLA/NRL [11]. Reprinted with permission from Hudson *et al.*, *Astron. Astrophys.* **453**, 433–446 (2006) [10]. Reprinted with permission from <http://chandra.harvard.edu/photo/2006/a400/> [11].

required [7,21]. In order to explore SMBHs hidden by thick absorbers (column density of neutral hydrogen (HI) $>10^{23}$ H/cm²), an energy range of 60–80 keV (in original rest frame) is required along with sufficient spatial resolution of 10–20 arcsec. Such attempts of these measurements have been done by balloon experiments, such as the International Focusing Optics Collaboration for μ Crab Sensitivity (InFOC μ S) [22], and later with the satellites the Nuclear Spectroscopic Telescope Array (NuSTAR) [23], and the International X-ray Astronomy Mission (ASTRO-H/Hitomi) [24]) with multilayer coatings (Pt/C or W/Si).

Surface slope errors in the optics affect the angular resolution of the telescope by changing the direction of converging photons, which redistributes the energy in the point spread function (PSF), degrading the ideal angular resolution based on the effective area. Surface roughness errors diffract light out of the focal points, reducing angular resolution as well. In optics considered for ATHENA, a 5 arcsec on-axis half-energy width (HEW) is the angular resolution requirement [25]. Table 2 shows the breakdown of the surface errors as a function of the spatial frequency at which they occur. Curvature errors (figure) contribute to a lengthening of the line focus created by x-ray optics, mid-spatial errors create local slope deviations, while the surface roughness and higher spatial frequency errors create scattering tails in the x-ray images.

The wide field of view (FOV) requirement of the telescope is primarily driven by the need to determine the distribution of supermassive black holes in the early Universe with enough samples in the covered FOV. To perform an efficient survey, which

Table 1. Overview of the X-Ray Space Optics Technology Needs to Meet the Science Goals of the Next Decade [7,12–18]^a

Specification	Requirement	Justification
Sensitivity	$\sim 10^{-17}$ erg cm ⁻² s ⁻¹ (0.5–2 keV, observed frame)	Survey of distant AGN
Effective area	>2.5 m ² at 1 keV, >0.65 m ² at 6 keV, >350 cm ² at 30 keV	Line spectroscopy and broadband spectrum
Angular resolution	≤ 5 arcsec, 10–20 arcsec	Detection of distant AGN mapping
Field of view	>200 arcmin ² (wide), 25 arcmin ² (narrow)	Black holes distribution cluster spectroscopy
Spectral resolution	$\Delta E < 3$ eV at 6 keV, $\Delta E < 150$ eV at 6 keV, $E/\Delta E \sim 3000$ (0.3–1 keV)	Dynamics of cluster gas redshift of Fe line absorption line features
Angle of polarization	1 deg/keV	Black hole spin
Stray light	5×10^{-4} rejection in 0.5–1.5 deg annular region	Eliminate unwanted images
Areal density	≤ 1 kg/m ²	Launch vehicle

^aEach parameter is chosen by the specific science goals of the instrument system. AGN, active galactic nuclei.

Table 2. Overview of the Spatial Frequency Surface Specifications for Proposed X-Ray Primary Mirrors That Will Meet the Science Requirements of the Next Generation of Space Optics [25–27]^a

Total surface error	<5 arcsec on-axis HEW
Figure (<4 cpa)	1.5 μ m PV
Mid spatial (4–60 cpa)	<1 arcsec slope errors
Roughness (5–500 mm ⁻¹)	<0.5 nm RMS

^acpa, cycles per aperture; HEW, half energy width; PV, peak to valley; RMS, root-mean-square.

requires a sensitivity of $\sim 3 \times 10^{-17}$ erg cm⁻² s⁻¹ (0.5–2 keV) in 200 ks, an observational area of >200 arcmin² is needed with the wide field imager. On the other hand, imaging spectroscopy observation of clusters with a calorimeter array requires a FOV of 25 arcmin² to cover the cluster core and surrounding background area [7].

The spectral resolution requirement for the next generation of x-ray telescopes varies significantly with each science objective. The need to trace the dynamics of hot gas in groups and clusters out to high redshift and to measure elemental abundances to sufficient accuracy drives the spatially resolved high-resolution spectral sampling to a requirement of $\Delta E < 3$ eV at 6 keV (narrow field imaging with the micro-calorimeter array) [7]. Better than 10 eV energy resolution is a key technology to distinguish fine structure of emission line features and the dynamics (>100 km/s), as was demonstrated in the test observation of the Perseus cluster with Hitomi XRS [28], which is equipped with a micro-calorimeter array cooled with liquid helium and/or coolers. In a wide field imaging scenario, for the science case of the growth of a supermassive black hole, a spectral resolution of 150 eV full width at half-maximum at 6 keV is needed to determine temperatures and centroid the Fe line for redshift measurements. The most stringent spectral resolution to obtain a resolving power of $E/\Delta E \sim 3000$ comes from point source dispersive spectroscopy requirements to measure lines in absorption against a continuum. This permits measurement of the cosmic web of baryons, where absorption lines in the range of 0.3–0.5 keV are expected in the continuum of a point source behind the warm-hot intergalactic medium (WHIM). In measuring the absorption lines, the missing baryons in the WHIM and their velocity structure can be determined. The existing measurements in these regimes are at the limit of instrumental detection thresholds, and therefore need confirmation and further investigation [29–33].

In contrast to the specifications of sensitivity, angular resolution, collection area, and spectral resolution, which are centered around faint objects, the next generation of x-ray telescopes will utilize the large effective collection area to perform time-resolved measurements from bright targets with a statistically high accuracy. Such time-dependent phenomenon, such as x-ray emission from neutron star systems, occurs on the time scale of 1 kHz, or several hundreds of hertz for black hole systems. Understanding the periodicity, or lack thereof, can place constraints on the black hole spins and neutron star compactness. These quasi-periodic oscillations probe the strongly curved spacetime around compact objects, placing limits on their mass, spin, and radius, which will hopefully lead to the determination of the equation of state in the high density limit [34–36]. Therefore, the time resolution and count rate capability of the future x-ray telescopes must be sub-millisecond resolution with more than 1 million events per second [7]. To further aid in determining the black hole spin, polarization measurements of black holes to detect a rotation of the angle of polarization, which is rotated due to relativistic effects for different observer orientations, will be made [37,38].

X-ray observations will provide fundamental insight into our Universe through the hot and energetic black hole science, mapping galaxy clusters while tracking their cosmological evolution in time and probing the extremes of our understanding of the event horizon surrounding a black hole. The optics technology required to make these telescopes is progressing to an amazing level of maturity and will continue to grow. By understanding the science goals set forth in the previous sections, we can view the space optics technology research in its broader context. We hope that this review of the current technology to fabricate, test, and assemble the next generation of x-ray space optics will enable further developments by learning from our scientific peers.

2.2. UV/Optical/IR Science

Astronomical science observations are not only made in the x-ray spectrum but also across the UV, optical (visible), and IR. This wavelength regime is host to awe-inspiring science that is possible only through its own class of space telescopes. As part of the *New Worlds, New Horizons* [1] document produced by the NRC, science goals for the coming decade necessitate many UVOIR measurements. Scientific research in areas that will benefit from advances in these space telescopes include the following: the search for the first stars, galaxies, and black holes in the universe; seeking exoplanets in the habitable zone of their parent star; and further understanding our own solar system. UVOIR astronomy will provide insight into questions of the nature, “When and how did the first galaxies and stars form? How did the first galaxies form quasars? What other worlds exist in the universe that could harbor life? What are the conditions of the various moons and planets within our solar system?” Through answering these questions, we will answer some of the most fundamental questions surrounding our existence. The discoveries made by the next generation of space optics in the UVOIR will inspire the world and create common bonds between all humanity by placing our Earth in the context of the Universe.

A top level flow down of the technology requirements for the next generation of UVOIR telescopes is given in Table 3. The aperture of the telescope is driven by light collection, angular resolution, and planet detection efficiency in searching for exoplanets in the HZ around stars. Shown in Fig. 2 is an image of four such planetary-mass objects orbiting a nearby star taken by the Gemini and Keck Observatories. Aperture size of the telescope impacts the efficiency of exoplanet detection in the HZ, where the number of detections scales as D^2 , where D is the diameter of the telescope aperture [42–44]. This yield is influenced by several astrophysical assumptions about the nature of the exoplanets: assumed size and optical properties (albedo, atmospheric composition, etc.) of the exoplanet, the exozodiacal dust cloud surface brightness [45], and the number of exoplanets per star [43]. Given that few to no observations of these parameters for exoplanets have been made, much is based on data from Earth [44]. To directly detect an exoplanet, the angular resolution of the telescope

Table 3. Overview of the UVOIR Space Optics Technology Needs to Meet the Science Goals of the Next Decade [7,12–18,39]^a

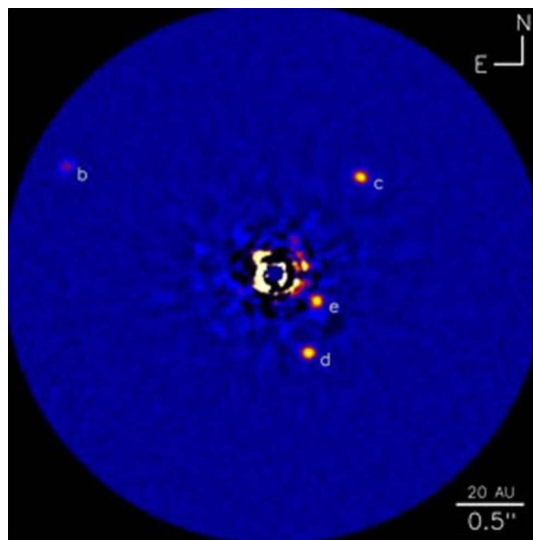
Specification	Requirement	Justification
Primary aperture	≥ 8 m	Resolution, sensitivity, exoplanet yield
Wavefront error	35 nm RMS WFE	Diffraction limited at 500 nm
Wavefront stability	0.01 nm RMS over 10 min	Exposure time
Angular resolution	2.74 milliarcsec/pixel	Cosmic origins (UV)
Pointing stability	~ 1 milliarcsec	Starlight suppression
Stray light	Zodiacal dust emission limited between 0.4 and 1.8 μm	Spectroscopy SNR
Total figure error	8 nm RMS	Symmetric PSF
Contrast in Coronagraph	10^{-10}	Starlight suppression
Inner working angle	$< 2\lambda/D$	Internal coronagraph
Outer working angle	$> 20-30\lambda/D$	Internal coronagraph
Starshade positioning	≤ 20 cm	Starlight suppression
	≤ 50	Delta IVH
	≤ 100	Falcon 9H
Areal density (kg/m^2)	≤ 300	SLS Block 1
	≤ 600	SLS Block 2
Telescope temperature	273–293 K	Thermal stability

^aEach parameter is chosen by the specific science goals of the instrument system. PSF, point spread function; RMS, root-mean-square; SLS, space launch system; UVOIR, ultraviolet/optical/infrared; WFE, wavefront error.

(determined by the aperture size) should be better than 0.5 times the angular radius of the HZ, which at a distance of 10 pc can range from 2.2 to 566 milliarcsec [15]. The required diameter of the telescope to achieve this angular resolution is evaluated at 760 nm because this wavelength is a key biomarker for life (molecular oxygen). Furthermore, sensitivity in the range from 500 to 800 nm is critical for determining the strongest markers of life as we know it on Earth [46]. The aperture size of the telescope also sets the collection area, or required observation time, to achieve a specific signal-to-noise ratio (SNR). To confidently detect exoplanets an $\text{SNR} = 10$ with a spectral resolution $R = 70$ is desirable. These driving and competing science goals of exoplanet detection leads to an aperture specification of greater than 8 m [12]. As the aperture diameter increases, the exoplanet yield and angular resolution increase, which creates an incentive for larger-aperture space telescopes.

To answer the questions posed by the scientific community, we must continue to develop new optics technology that will enable the space optics to make astronomical measurements. The requirements on the next generation of UVOIR telescope surface errors are summarized in Table 4. The general astrophysics goal of Cosmic Dawn and Physics of the Universe—to find the first stars, galaxies, and black holes—requires diffraction-limited performance with a symmetric PSF in the visible spectrum, which generally drives the low-spatial frequency surface specifications [15]. Here we define the widely used and often ambiguous term “diffraction-limited” as meaning a Strehl ratio greater than 80%, where the Strehl ratio is the ratio between the illumination at the center of an aberrated point image to an aberration-free point image (e.g., Airy pattern [47]). Low- to mid-spatial frequency errors (traditional aberrations) move energy from the core of the PSF to the outer rings, reducing the Strehl ratio and

Figure 2



Adaptive optics image of four planetary-mass objects (b)–(e) orbiting the A-type star HR8799 captured by the Gemini and Keck II Observatory using the angular differential imaging technique. The direct illumination from the star was subtracted so that the faint exoplanets could be detected, showcasing the need for extreme suppression in future UVOIR space telescopes. Image credit: National Research Council of Canada-Herzberg Institute of Astrophysics, C. Marois and Keck Observatory. From Marois *et al.*, *Science* **322**, 1348–1352 (2008) [40]. Reprinted with permission from AAAS. Reprinted by permission from Macmillan Publishers Ltd.: Marois *et al.*, *Nature* **468**, 1080–1083 (2010) [41]. Copyright 2010.

degrading image quality [48]. Furthermore, stability of the PSF over multiple measurements is critical for the general astrophysics astronomy science in the UVOIR spectrum [49–51]. The New Worlds objective—to identify exoplanets—often necessitates smooth surfaces to suppress scattering, which sets the mid- to high-spatial frequency surface requirements. Errors in this spatial frequency regime push energy from the core of the PSF into the tails of the distribution. This destroys the desired contrast when performing exoplanet detection and characterization. The surface specification for the future UVOIR telescopes is based on a -2.25 power spectral density (PSD) slope, leading to a total surface error of 8 nm RMS, which is broken down into specific spatial frequency regimes. For the low-order errors, <4 cycles per aperture (cpa), 5.5 nm RMS is needed, at 4–60 cpa (mid-spatial), 5 nm RMS, in the high-spatial regime (60 cpa to 100 $\mu\text{m}/\text{cyc}$), 1.5 nm RMS, and a roughness (<100 $\mu\text{m}/\text{cyc}$) of ~ 0.5 nm RMS is specified [12,15].

To directly detect exoplanets, in which light from the parent star is reflected by the exoplanet, suppression of the direct starlight with a contrast ratio of 10^{-10} is necessary. Only a space-based telescope can achieve this since ground telescopes are limited to approximately 10^{-8} due to atmospheric turbulence [52]. While this level of suppression may be sufficient for future extremely large ground-based telescopes with significant post-processing of the data [53], the most likely, and efficient, means of characterizing exoplanets is with space telescopes. The extreme level of starlight suppression will be achieved using an optical occulter, either in the form of an external starshade [54–56] or an internal coronagraph [57–59]. The direct light from a star is blocked by the starshade by minimizing the diffraction pattern in the region of the telescope's aperture. If the planet–star system is assumed to be observed at a distance of 10 pc, the separation angle between the two objects is 0.1 arcsec. A proposed flower-shaped starshade will fly at approximately 50,000 km away from the telescope and have about a 30 m diameter, which will subtend 0.05 arcsec in the telescope's field of view [60,61]. This generates a diffraction pattern where the on-axis radiation from the star in the main detection band (500–800 nm) [12] is minimized. On the other hand, a coronagraph operates internally at the instrument level by removing the direct light from the parent star within some specified angular annulus [62]. To accomplish this, the point spread function is altered such that the on-axis starlight is redistributed, creating a donut of high contrast, which is defined by its inner and outer working angle. The smaller the inner working angle (IWA), the closer to the parent star an exoplanet may be detected [63]. Therefore, it is important for the next-generation space telescopes to have a small IWA of $<2\lambda/D$, where λ is the wavelength and D is the aperture of the telescope. A larger outer working angle (OWA) is also desirable to achieve a large high-contrast angular region, which drives the OWA specification to greater than $20\text{--}30\lambda/D$. In contrast, a starshade diffracts the light from the on-axis star outside of the telescope aperture, thereby removing the much brighter source. To be a viable starshade occulter, it must fit within the launch vehicle and achieve positioning accuracy of ≤ 20 cm [60]. The starshade must have low scattering

Table 4. Overview of the Spatial Frequency Surface Specifications for Proposed UVOIR Primary Mirrors That Will Meet the Science Requirements of the Next Generation of Space Optics^a

Total surface error	~ 8 nm RMS
Figure (<4 cpa)	~ 5.5 nm RMS
Mid spatial (4–60 cpa)	~ 5 nm RMS
High spatial (60 cpa to 100 $\mu\text{m}/\text{cyc}$)	~ 1.5 nm RMS
Roughness (<100 $\mu\text{m}/\text{cyc}$)	~ 0.5 nm RMS

^aThe specifications were based on a -2.25 PSD slope [12,15]. cpa, cycles per aperture; RMS, root-mean-square.

at its edges, so as to not generate stray light problems, creating the requirement that the edge radius of curvature (RoC) should be $\leq 10 \mu\text{m}$ [64] and an edge specular reflectivity $\leq 10\%$.

During an observation, which can last for many hours, the wavefront error of the telescope must be very stable such that high-contrast imaging is possible. As the wavefront error of the telescope changes over a measurement, the recorded image smears and blurs, resulting in a loss of information. This is especially critical for internal coronagraphs, which need a stable wavefront in order to create the annular region of starlight suppression. Once the dark region is formed, wavefront error stability of $\sim 10 \text{ pm}$ RMS per control step is needed [65–67]. Low-order aberrations—piston, tip, tilt, power, coma, astigmatism, and spherical aberration—will be important to correct to obtain the desired stability. The factors contributing to the wavefront error come from mechanical, thermal, and dynamic properties of the telescope. The stiffness and mass of the telescope affect how vibrations propagate into the optical performance, while thermal gradients can cause shifts in the optical components and dynamic variation from reaction wheels or micro-thrusters input additional optical aberrations. To limit these effects, the next generation of space telescopes should achieve a thermal stability of a few pm/K over a gradient of a few mK at room temperature. Depending on the material chosen for the support structure and telescope substrate, the thermal control can range from 0.1 to 1 mK, where greater thermal stability is needed for materials with larger variability with temperature (coefficient of thermal expansion, thermal conductivity, etc.).

A launch vehicle for the observatory places limits on the aperture size, but more critically, the areal density of the mirrors. Depending on the launch vehicle, the payload size varies significantly, so the areal density also fluctuates greatly for each aperture size and vehicle [15]. The James Webb Space Telescope (JWST) mirror defines the state of the art with a primary mirror areal density of 65 kg/m^2 and assembly of 1600 kg, which is planned for launch on an Ariane V rocket with a payload of 6600 kg. Future UVOIR telescopes may be launched via a Delta IVH with an allocation of 2500 kg for the primary mirror, or Falcon 9H with 5000 kg, or Space Launch System (SLS) Block 1 with 15,000 kg, or finally a SLS Block 2 with 30,000 kg. Therefore, given the variation in launch vehicle payload, the required areal density also changes depending on which vehicle is chosen. By selecting the SLS Block 2 vehicle, the mirror areal density provided by current ground-based telescopes may be sufficient for future space optical telescopes [39]. This is attractive from a cost and technological standpoint since the fabrication processes have already been developed and proven for the ground applications.

2.3. Mid- to Far-Infrared Science

The MFIR spectrum is host to a multitude of critical information to help us understand the Universe. Observations in the MFIR allow us to see through interstellar dust, identify galaxies with large amounts of new stars, characterize the emission mechanisms present in AGN [68], observe cool objects, and perform atomic, ionic, molecular, and solid-state spectroscopy [69]. Previous space telescopes in the MFIR, such as the Infrared Astronomical Satellite AKARI (ASTRO-F) [70] or Spitzer [71], have furthered our understanding of the Universe and pushed the capability for exploration of the cosmos in the infrared. A future telescope, the Space Infrared Telescope for Cosmology and Astrophysics (SPICA) [72], will probe the formation and evolution of planetary systems, the life cycle of dust in the Milky Way and nearby galaxies, the AGN/starburst connection over cosmic time and as a function of the environment, and many other science objectives. Data from these measurements has helped shape our fundamental understanding of the formation of the Universe, as shown in Fig. 3.

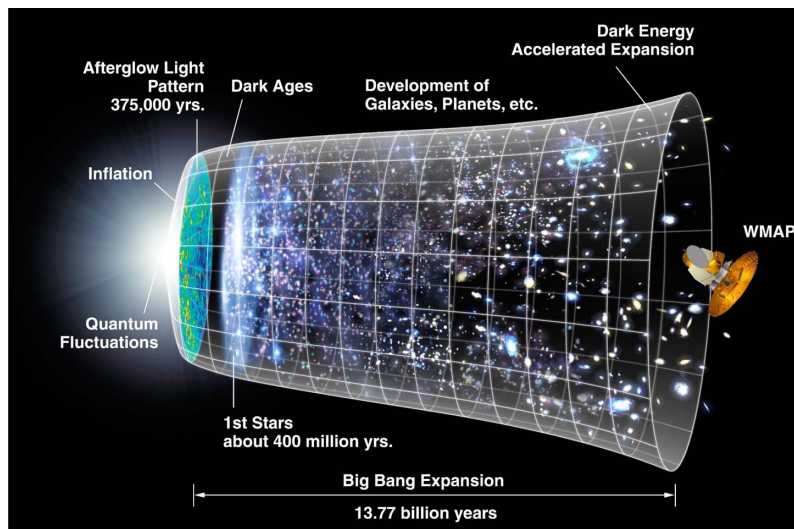
A proposed mission, the thinned aperture light collector (TALC), will further the light collection capabilities, allowing astronomers to detect fainter and smaller objects in the far-infrared to sub-millimeter spectrum [73–75].

The questions answered by these investigations are only accessible through the MFIR spectrum, which poses some unique challenges compared to the x-ray or UVOIR telescopes being developed concurrently. A top-level overview of the technology requirements for the next generation of MFIR telescopes is given in Table 5. The telescope operational temperature, wavelength coverage, and image quality requirements separate the science made possible by the MFIR from other frequency bands. A next-generation MFIR telescope should cover wavelengths from 5 to 210 μm , with a possible extension into the mid-infrared spectrum down to 3.5 μm to achieve direct detection of exoplanets. This is to complement the current suite of instruments on Herschel, operating in the wavelength range of 55–671 μm [76].

To achieve better science outcomes compared to the current generation of telescopes, the diameter of the telescope should match or exceed that of the present observatories. Furthermore, the science objectives drive the aperture to be at least 3 m in diameter, which is comparable to Herschel's 3.5 m aperture [77]. The angular resolution and light collection of the telescope are set by the diameter, which is particularly important for the characterization of exoplanets. MFIR surveys are limited in depth by a fundamental confusion due to a high density of faint galaxies distributed approximately isotropically within the field of view. The noise limit created by these extragalactic sources, quantified with a source density criterion [78], varies with the inverse square of the diameter of the telescope. Therefore, by increasing the diameter, the fundamental limits of confusion are reduced.

Telescope diameter also determines the limit of resolution through diffraction from the primary aperture. The image quality should be diffraction limited at 5 μm over a center field of view of 5 arcmin radius, while the diffraction limit should be maintained at 30 μm over a 10 arcmin radius in order to maximize the angular resolution offered

Figure 3



Cosmic timeline shown as a plot of the rate of expansion of the Universe as the width. MFIR measurements with space telescopes will provide more data and answer many questions concerning the history of the Universe. Image credit: NASA Wilkinson Microwave Anisotropy Probe (WMAP) Science Team.

for the given aperture. Through a diffraction-limited performance, future MFIR telescopes will resolve details of the roles that stellar populations play in heating dust, and many other fine scale deficiencies encountered in past observatories [79,80]. A stricter image quality metric is needed over the center field of view in order to satisfy the mid-infrared instruments for exoplanet detection. The corresponding wavefront error to achieve the diffraction-limited performance at 5 μm is less than 350 nm RMS. The wavefront error (and therefore the surface error, which is the half of the wavefront error considering the double-path in reflection) can be broken down in to specific spatial frequency regimes [81]. These details are shown in Table 6. In general, the low-spatial frequency errors can be spread equally between focus and higher-order aberrations (pushing into the mid-spatial frequency regime) so long as the total error is within the wavefront budget. However, a recommendation is to keep the total surface error to below 175 nm RMS. The high-spatial frequency surface error budget, which induces wide-angle scattering, is determined by the stray light needs of the telescope.

To meet the science objectives of characterizing the formation and evolution of planetary systems, galaxies, and the life cycle of dust, the sensitivity of MFIR telescopes must be increased. By reducing the background photon noise generated by the telescope, the signal-to-noise ratio is improved and more faint objects can be detected. Background sky should limit the sensitivity of the telescope, not the emission of the structure or mirrors themselves. A strong dependence of background noise with telescope temperature exists due to the blackbody emission spectrum of an object. Therefore, a telescope temperature of ~ 6 K is required to achieve the background sky limit for wavelengths below the science band. However, as thermal gradients and temperature fluctuations will occur, an upper limit of 10 K hot spots is desirable.

The sensitivity of the telescope is also affected by stray light sources, which are generated from unwanted reflections or light paths through the telescope [82]. Once again, the goal is to have the sensitivity of the telescope limited by the background sky emission, which requires a stray light rejection level of 90% [83–86]. This means

Table 5. Overview of the MFIR Space Optics Technology Needs to Meet the Science Goals of the Next Decade [7,12,13–18,72]^a

Specification	Requirement	Justification
Wavelength range	3.5–210 μm	Exoplanet detection
Aperture	>3 m	Angular resolution and light collection
Performance	Diffraction limited at: 5 μm over 10 arcmin, 30 μm over 20 arcmin	Maximum angular resolution
Angular resolution	100 milliarcsec	Galaxy, star, and planet formation
Field of view	12 arcmin radius	All sky survey
Telescope temperature	<6 K, 10 K hot spots	Noise sources

^aEach parameter is chosen by the specific science goals of the instrument system. IR, infrared; SNR, signal-to-noise ratio.

Table 6. Overview of the Spatial Frequency Surface Specifications for Proposed MFIR Primary Mirrors That Will Meet the Science Requirements of the Next Generation of Space Optics^a

Total surface error	175 nm RMS
Figure (<3 cpa)	<125 nm RMS
Mid spatial (3–1,000 cpa)	Not specified
High spatial (>1000 cpa)	<17.5 nm RMS TIS <0.2%

^aNote that the surface errors are half the wavefront errors [72,81]. cpa, cycles per aperture; RMS, root-mean-square; TIS, total integrated scatter.

that out-of-field sources (artificial and natural) will not increase the observed patch of sky background signal by more than 10%.

2.4. Synopsis of Science Drivers

In general, to provide a space optical system that will meet the science goals outlined in the Decadal Survey, a large-aperture, low-areal-density, high-stiffness, and thermally stable mirror is required. The surface errors must be controlled across all spatial frequencies, and the thermal and mechanical stability of the telescope on orbit must be carefully engineered. The top-level technology flow-down requirements within each major wavelength regime are summarized in Tables 1–6. We note that this summary cannot represent all requirements but serves as a good overview to put the reviewed technology in context. Advancements in space optics technology based on past missions at space agencies across the globe [87] have been made such that key hardware systems are realizable [88].

3. LARGE LIGHT-WEIGHTED MIRROR FABRICATION

Creating an astronomical telescope mirror is an extremely unique task, especially considering the specifications that are desired for the next generation of telescopes. Only a handful of companies and institutions are capable of the size, finish, and quality because of the vast range of high-precision skills required to make astronomical telescopes [89]. These fabrication facilities must produce primary and secondary mirrors for the telescopes, which necessitate unique technologies due to different base radii of curvature (i.e., concave primary versus convex secondary).

The primary mirrors identified as viable candidates to be used in the next generation of space optics require novel fabrication methods due to their sheer size, stiffness, mass, thermal conductivity, and substrate material. As identified in the Science Instruments, Observatory and Sensor Systems Technology Roadmap (technology area # 8) by NASA's Office of Chief Technologist [16,90], large-aperture diameters, low areal densities (launch vehicle dependent), and high stability are required to meet the science objectives in the next decade. Achieving the desired surface accuracy across the large light-weighted aperture of the mirror requires new technologies from the start of the fabrication process to the final stages of polishing. A list of the proposed surface specifications for the primary mirror of a telescope used to meet the science goals are given in Tables 2, 4, and 6. The specifications cover the full range of spatial frequencies found on the optical surface, which are usually expressed using a PSD [91,92] or a structure function [93,94]. The areal density and thermal stability requirements in Tables 1, 3, and 5 limit the materials used to fabricate the primary mirror. Given the ambitious requirements on the telescope, improvements in the fabrication process from the base substrate manufacturing, during rough grinding, to final polishing/figuring have been investigated. We will now provide a sampling of these technologies broken into sections according to the stage at which they take place in fabrication.

3.1. Producing a Stiff, Light, and Low Expansion Mirror Substrate

The substrate of the primary mirror determines many optical and mechanical characteristics of the entire telescope and must be carefully selected to ensure that the mission goals are met. The type of material also changes the fabrication methods available, which affects cost, manufacturing time, and risk. Given in Table 7 are the critical parameters of the current methods of manufacturing the substrates of large telescope primary mirrors.

3.1a. X-Ray Optics Substrates

X-ray optics require a significantly different fabrication process compared to UVOIR or MFIR telescopes since they are designed to operate at shallow incidence angles instead of normal incidence. In order to produce a large-area x-ray telescope for ATHENA where the physical mirror area exceeds 500 m² when taking into account the <0.5 degree grazing angle of incidence, technologies that do not require special post-polishing processes are needed. Two promising technologies exist for future x-ray telescope optics, either slumped glass optics (SGO) or silicon pore optics (SPO) [106]. Both materials exhibit the required characteristics of mid-spatial frequency and roughness errors as listed in Table 2. The mid-spatial specification satisfies the slope error requirements, contributing much less than 5 arcsec of total HEW errors while the roughness specification will not produce significant scattering in the tails of the x-ray images. The figure errors are controlled via a slumping or molding process to produce a total peak-to-valley (PV) less than 1.5 μm. Given in Fig. 4 are examples of (a) SGO and (b) SPO optical stacks that will be replicated to form the full optical surface. A preliminary SGO technology was used for the optics in NuSTAR [108], while new developments in the technology might be implemented on optics for the ATHENA mission [23,109]. The principle of making an SGO is that of a molded sheet of glass pressed and heated such that either the optical or non-optical surface is in contact with the mold. Multiple sheets are glued together with ribs formed from glass or graphite. The ribs ensure that each mirror shell is stacked with the correct shape and position, aiming to reach 5 arcsec image quality, while also providing mechanical stiffness. Each stack of slumped glasses will then be combined in a given geometry to form the final optical assembly. The SPO technique also relies on creating the full aperture from multiple segments of stacked optical surfaces [107]. In this method, silicon wafers produced for the semiconductor industry are utilized for their well-controlled uniformity and polished surfaces. The wafers in SPO are etched from the back side to leave ribs to keep the correct distance to adjacent wafers. They are then pressed into a mold to give the required radius of curvature, creating a bond between sheets via a strong chemical covalent bond of hydroxyl groups [96] instead of glue. The surfaces are elastically bent and their roughness is not affected by the quality of the mandrel [95].

Table 7. Overview of Some Promising Substrate Materials and a Sampling of the Critical Characteristics to Meet the Requirements of the Future Space Telescopes^a

Technology	Areal Density (kg/m ²)	Diameter (m)	CTE (ppb/K)	1st Frequency (Hz)	Fabrication Method
X-ray					
SPO [95,96]	0.5	0.066	2600	–	Stack and bonding
SGO [23,97]	0.5–1.0	0.2	2000– 7200	–	Hot slumping
UVOIR					
ELZM [98]	25–75	1–4	1	450–75	CNC Grinding
Stacked core [88,99]	35–60	1.5–8	15	450–33	AWJ, CNC, and slumping
ULE segments [100]	40–60	1–2	15	–	CVD and CNC Grinding
Spin cast [101]	~300	~4.2–8.4	2800	–	Glass melt
MFIR					
Sintered SiC [102,103]	14	0.7–4	2200	321	Sintering with CVD coating
SiC sandwich [104]	–	2	4000	100	Additive manufacturing
CFRP [105]	1.53	2	–	–	Resin coated

^aNote that spin-cast mirrors have been used not in space telescopes but for ground-based observatories. Blank entries were not reported in the literature. SPO, silicon pore optics; SGO, slumped glass optics; CTE, coefficient of thermal expansion; ELZM, extreme light-weighted ZERODUR mirrors; CNC, computer numerically controlled; AWJ, abrasive water jet; CVD, chemical vapor deposition; CFRP, carbon fiber reinforced plastics.

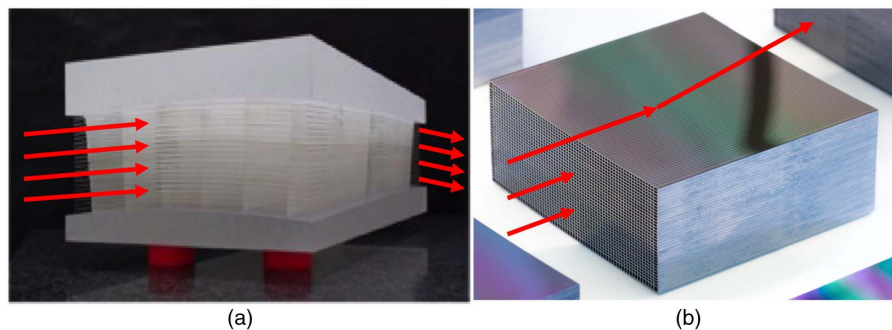
3.1b. UVOIR Mirror Substrates

A UVOIR telescope requires very-large-aperture primary mirrors with low areal density, requiring novel technologies to produce mirror substrates with sufficient mechanical properties along with the optical. Two main fabrication thoughts on obtaining large mirrors exist: combine many small-diameter mirrors or a few large mirrors [110]. In both cases, new enabling technologies to meet the requirements given in Tables 3 and 4 have been developed to produce high-quality optical substrates.

A monolithic substrate fabrication method called extreme light-weighted ZERODUR mirrors (ELZMs) is a technology that uses a substrate material produced by Schott in a monolithic structure that is then machined to light-weight the mirror [98]. To increase the diameter of the substrate while maintaining the appropriate stiffness and areal density, very deep pockets and ribs must be machined in to the back side of the mirror. This poses a technical challenge of safely and effectively grinding, which is circumvented by using a different method called stacked core [99]. In this technique, smaller and more readily fabricated cores are produced and then fused together to form a deep pocket and expand the diameter of the surface. This reduces the risk of manufacturing failure because the individual sections can be remade. A front and back plate are used as a sandwich to the cores. The entire mirror is then slumped to the correct base radius of curvature. Another sandwich type substrate is made by additive manufacturing, which enables complex structures within the substrate [104,111]. A similar idea is employed in the ultra-low expansion (ULE) glass segmented method where hexagonal pieces of glass are combined together to form the full aperture [100]. To form the hexagonal segments, chemical vapor deposition (CVD) generates a glass boule (rough cylindrical base structure) that is machined into the correct dimensions and given the base radius of curvature.

A monolithic surface with light-weighting can also be made using a spin-casting technique [101], but so far due to the materials used in the process, it has not been applied to a space telescope. The type of glass required in the spin-casting process does not have an extremely low (comparable to the ZERODUR or ULE) coefficient of thermal expansion (CTE), but very large and stiff mirrors have been produced.

Figure 4



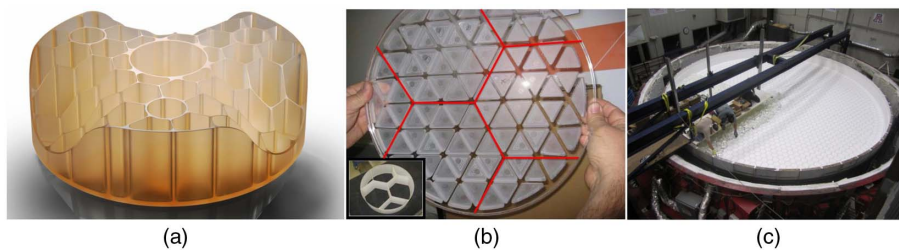
Optical stacks of x-ray mirrors formed using (a) a slumped glass optics stack of ~ 20 slumped glass sheets with graphite spacers. Image credit: INAF-Astronomical Observatory of Brera. Reprinted with permission from Salmaso *et al.*, Proc. SPIE **10563**, 105639 (2017) [23]. (b) Silicon pore optics stack of ~ 40 silicon wafers with numerous ~ 1 mm square pores as seen on the left face. Image credit: Cosine measurement systems. Reprinted with permission from Collon *et al.*, Proc. SPIE **9905**, 990528 (2016) [107]. Red arrows show the approximate x-ray paths of each stack.

Shown in Fig. 5 are three different substrate technologies that are considered in UVOIR astronomical primary mirrors: ELZM, stacked core, and spin-cast methods. In all cases, the light-weighting to achieve a low areal density while maintaining good structural performance is critical and is achieved with a variety of methods.

3.1c. Mid- to Far-Infrared Optics Substrates

For space telescopes in the MFIR wavelength regime, a technique using carbon fiber reinforced plastic (CFRP) mirrors shows promise to produce large, low CTE, and light mirrors [105]. In this method, a base substrate of resin and carbon fibers are laid down in a random orientation, resulting in a light and stiff structure. To form an optical surface suitable for polishing, a thin (e.g., 40 nm) layer of SiC is deposited on the surface. Another CFRP process covers the substrate using a nanolaminate reflective facesheet that is deposited by sputter deposition [113]. The CFRP substrate mirrors are made using a replication method, which does not require grinding or polishing to achieve low roughness surfaces while other methods must be post-processed. Sintered SiC [102] is also an attractive manufacturing process due to the mechanical and thermal properties of the substrate. To use the sintered SiC, which is porous, in visible applications, a layer of non-porous SiC is added on top via CVD to achieve roughnesses down to 0.1 nm RMS. To create large monolithic surfaces, segments of SiC can be brazed together either before or after the CVD process, depending on the intended application [114,115]. The mechanical structure of the telescope can also be machined from sintered SiC, creating a highly stable structure. The Gaia mission of ESA is utilizing a 3 m quasi-octagonal support structure of sintered SiC [116]. The SPICA mission from JAXA will utilize a form of SiC mirrors, either sintered SiC, reaction-sintered SiC, or carbon fiber reinforced SiC [117]. Shown in Fig. 6 are two examples of sintered SiC and carbon fiber reinforced SiC that are promising technologies for future MFIR space telescope missions. Meanwhile, the JWST mirror segments were made from optical-grade beryllium. The beryllium starts as a powder, which is placed in a container shaped to the nominal mirror. The powder is subjected to hot isostatic pressing to convert the powder to a solid form. The container is then

Figure 5



Three examples of substrates used in large UVOIR telescope primary mirrors. (a) Extreme light-weighted ZERODUR mirror (ELZM). Image credit: SCHOTT. Reprinted with permission from <http://www.us.schott.com> [112]. (b) Stacked core with glass facesheets. Image credit: H. P. Stahl. Reprinted with permission from Matthews *et al.*, Proc. SPIE **9143**, 91431U (2014) [99]. (c) Spin-cast light-weighted glass. Image credit: H. M. Martin. Reprinted with permission from Martin *et al.*, Proc. SPIE **8450**, 84502D (2012) [101]. Each technology uses a light-weighting technique to reduce the mass of the optic, which is critical for launch vehicle choice. Furthermore, new developments to mitigate the risks of manufacturing are being developed, such as those demonstrated in (b) where the backing structure is formed by fusing multiple cores together.

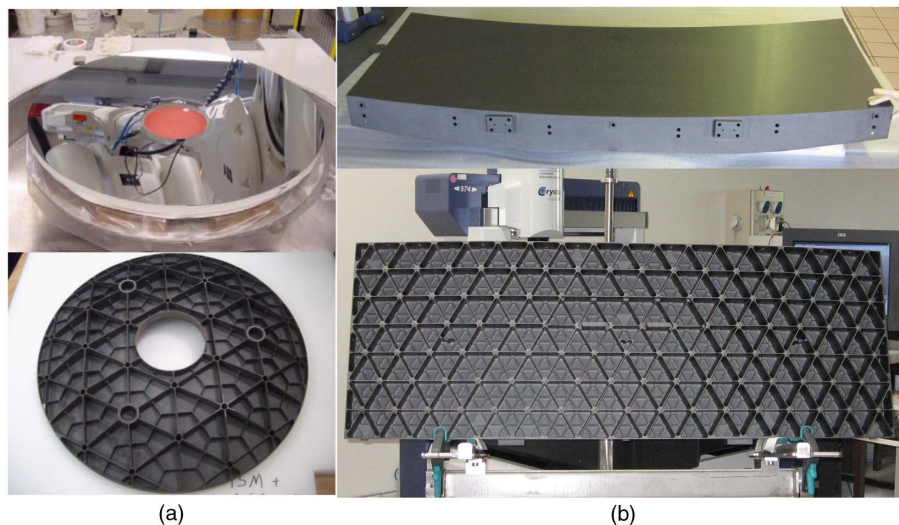
etched away to reveal the mirror substrate, which can be machined and light-weighted afterwards [118].

Further work is required for all the substrates listed above before they are ready to be used in the next generation of space telescopes. However, the current state of the technologies is very promising and the knowledge gained from developing them so far is invaluable. Developments in manufacturing and material science will enable the telescope mirrors to meet their performance goals. Unconventional methods for creating a large-diameter far-infrared telescope primary mirror are also being explored due to the size limitations of the current methods (JWST, SPICA, etc.). The TALC is one such project that uses a deployable 20 m primary based on stacking segments rather than folding [73–75]. This provides a more efficient means of obtaining high angular resolution per use of volume compared to previous designs.

3.2. Grinding, Polishing, and Figuring Processes

Once the substrate has been produced, it moves on to grinding and figuring to generate the overall surface features required for the optical performance. The grinding step removes material quickly and efficiently in order to minimize the amount of time spent polishing. During the grinding phase, material is removed at a much faster rate (e.g., ~ 1000 times faster during a fine grinding phase) compared to polishing and figuring. Therefore, accurate grinding methods are key to enabling the next generation of telescopes. Polishing is required after grinding in order to produce a smooth surface that meets the PSD requirements and to remove sub-surface damage caused by previous manufacturing processes. A well-polished surface is critical for the science goals because it determines the shape of the PSF, which affects image quality and therefore the end science information content. Many methods of grinding and polishing exist that are tailored to change the amount of removal and surface finish. Typically, high removal rates lead to a rougher surface and therefore more time is spent as the surface

Figure 6



Two promising technologies for the future MFIR space-based telescopes: (a) carbon fiber reinforced SiC, where the light-weighted backing of the mirror is shown below the optical surface. Image credit: H. Kaneda. Reprinted with permission from Kaneda *et al.*, Proc. SPIE **6666**, 666607 (2007) [117]. (b) Sintered SiC, shown waiting to be coated with CVD. Image credit: M. Bougoin, Mersen Boostec. Reprinted with permission from Bougoin, Proc. SPIE **10565**, 105652C (2017) [116].

gets closer to completion. Furthermore, with many telescopes utilizing off-axis designs, the grinding and polishing method must accommodate varying local curvatures and surface profiles. With these requirements, many tools and techniques have been developed to accomplish the job of grinding and polishing space telescope optics. We will now present a sampling of some key enabling processes in this field.

3.2a. Primary Mirror Surfaces

The JWST primary mirror array is composed of 18 irregular hexagonal segments. There are three different segment types, each with a unique off-axis prescription due to the change in location within the aperture. The mirror substrates are O-30 beryllium [119], specially formulated and produced for JWST. Beryllium is challenging to use in fabricating optical elements for several reasons. First, the material can be toxic if small particles enter the airways, which requires extensive safety procedures when being machined [120]. Further, material removal rates are low, surface pitting is precarious, and the material is stress-sensitive even for typical process stresses. All of these challenges are balanced against numerous advantages that are critical to the success of the telescope. The light-weighted structure has a high specific stiffness, the CTE is reasonably low (~ 11 ppm/K) at cryogenic space temperatures around 40 K. The segment-specific thermal deformations due to change in environment between fabrication and use can be measured and applied as a “backout” during optical metrology. In addition, finite element analysis simulations to remove the effects of gravity on Earth can be removed when creating hit maps for the segments during the iterative measure/polish sequence. Each segment type requires a different fabrication procedure in order to generate the aspheric surface profiles of the outer segments. The surface profile accuracy was enabled by computer-controlled optical surfacing, from the grinding stage to the polishing. Shown in Fig. 7 is an aluminum (Al) test surface used to verify the grinding process. Parameters used during processing of the beryllium mirrors are strongly proprietary, and therefore were not shared with the community.

The recently completed Daniel K. Inouye Solar Telescope (DKIST) by the Optical Engineering and Fabrication Facility at the College of Optical Sciences used ZERODUR as its substrate, was 4.2 m in diameter, and had a superpolished surface. Understanding the process parameters for the specific material in question is important

Figure 7

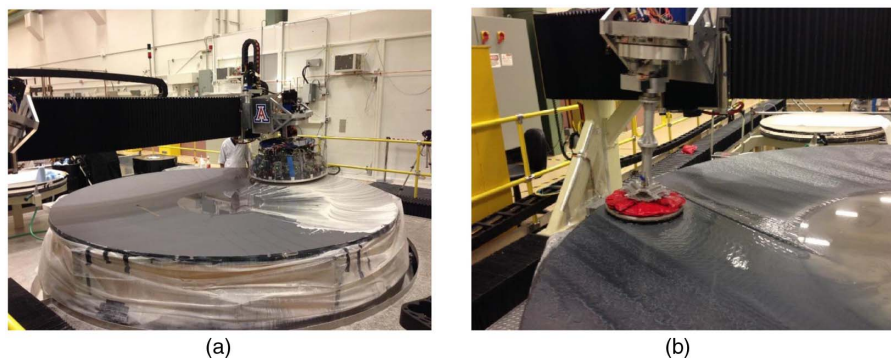


Aluminum surrogate of a JWST hexagonal segment during grinding tests at Tinsley on their computer-controlled optical surfacing machine. Image credit: J. C. Cole. Reprinted with permission from Cole *et al.*, Proc. SPIE **6265**, 62650V (2006) [120].

for removal rates and convergence [121]. To obtain low surface roughness across the full aperture, the surface was generated with a D64 Diamond Wheel by Schott, rough ground using 40 μm alumina, fine ground with 25–12 μm alumina, and polished with cerium oxide compounds. Various tool sizes, both active and passive, were used to accommodate the large aspheric departure of the surface. A 600 mm diameter stressed lap with 12 active bending actuators conforms to the varying local surface profile. A passive 300 mm flexible lap was designed to obtain maximum smoothing and final figuring [122,123]. An in-process polishing with these tools is shown in Fig. 8. Both laps were controlled via a computer in real time with orbital motion while the mirror rotated underneath. The mirror was measured to have a surface figure error RMS of <18.8 nm, which describes the RMS difference between the ideal mirror shape and the measured surface across the full aperture, and a micro-roughness of 1.05 nm RMS, which represents the high spatial frequency surface variations in locally sampled spots. A proposed specification for UVOIR primary mirror surface figure error RMS is <7 nm RMS [12], which is divided into spatial frequency regimes: (low/figure) 5.5 nm at <4 cpa, (mid-to-high) 5 nm at 4 to 60 cpa, (high) 1.5 nm at 60 cpa to 100 $\mu\text{m}/\text{cycle}$, and (micro-surface roughness) <0.5 nm at <100 μm . Obtaining this level of roughness on a large-aperture telescope moves the entire science community closer to producing surfaces that will enable the science goals of the future.

Producing many high-quality mirrors for the use in a large segmented telescope is a challenge for the manufacturing processes due to the high volume and precision. The European Extremely Large Telescope (E-ELT) developed a methodology to reduce the processing time of their 1 m class segments by implementing a low-damage precision grinding to achieve most of the removal, thereby saving time during the polishing and figuring stages [124]. In contrast to the grinding machines used in the DKIST fabrication, the E-ELT machines were optimized for small slope surfaces; shown in Fig. 9 is an E-ELT segment in the grinding process. The grinding stage achieved form accuracies of the order of $\pm 1 \mu\text{m}$ peak-to-valley with a surface roughness of 100–200 nm RMS and sub-surface damage less than 10 μm [125]. A variety of diamond grit sizes on resin bond wheels were used during the rough to finish stages, employing electroplated diamond grit wheels with an aluminum oxide compound for the forming stage.

Figure 8

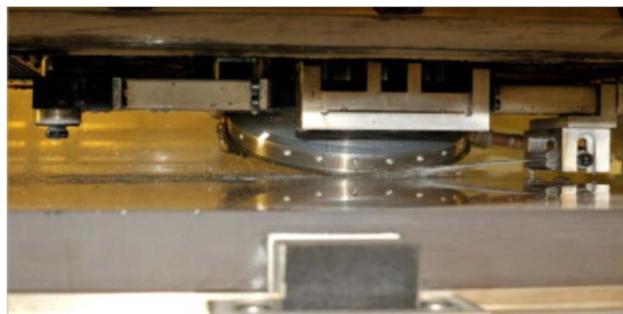


Polishing technologies used on the 4.2 m DKIST primary mirror made of ZERODUR to generate a superpolished final surface shape error of <18.8 nm RMS and a roughness of 1.05 nm RMS. Shown in (a) is the 600 mm diameter stressed lap where (b) shows the 300 mm diameter flexible lap. Image credit: C. J. Oh. Reprinted with permission from Oh *et al.*, Proc. SPIE 9912, 99120O (2016) [122].

Ion beam figuring is an alternative to traditional polishing methods and achieves very low surface roughness, which has been implemented on 1–2 m class telescope mirrors [126]. This process removes material from the surface by bombarding the substrate with a beam of high-energy (~ 1 keV) ions, which creates a Gaussian profile removal function with a peak of about 100–400 nm/min depending on the beam energy and parameters. The removal function is stable for many hours, which results in extremely well-controlled and predictable figuring. Hexagonal ZERODUR substrates for the E-ELT were ion beam polished to achieve a surface roughness reduction from 100 nm RMS to 4 nm RMS [127]. Achieving this level of surface roughness means that the segmented large-aperture telescopes have potential to meet the requirements dictated by the allowable amount of large angle scattering. A similar order of magnitude surface roughness is achieved on the sintered SiC substrates using a proprietary method, which can polish the CVD SiC to 9 nm RMS [128]. This greatly expands the areas of use for the SiC substrate, where the bare porous SiC cannot be polished to visible quality surface roughness. Very low surface roughness can also be achieved during polishing by utilizing magnetorheological finishing on 1 m class glass, ceramic, and single crystal materials [129].

Large aperture diameters are a critical parameter for the future space optical telescopes, which is also one of the most difficult challenges when fabricating monolithic primary mirrors. While material selection determines the areal density, thermal and mechanical properties of the substrate, the technology to polish across an 8 m diameter mirror is equally important. The Richard F. Caris Mirror Lab at the University of Arizona has technology in the area of grinding and polishing very-large-aperture monolithic mirrors for ground-based telescopes [130,131]. The same skills developed and knowledge gained from their projects can be applied to the fabrication of space optics. A recently completed project polishing the combined primary and tertiary mirrors of the Large Synoptic Survey Telescope showcases the tools required to obtain about 20 nm RMS error across an 8.4 m aperture [132]. Three tools were used in the polishing process: a 1.2 m stressed lap [133] with bare pitch or synthetic polishing pads, a rigid-conformal (RC) lap of diameters 35–12 cm based on a non-Newtonian fluid that conforms to the global freeform shape while staying rigid locally [134], and a small pitch lap of diameter 10–5 cm covered with a synthetic polishing pad. For the current project of the 8.4 m diameter Giant Magellan Telescope (GMT) mirror segments, a freeform generating machine is used to generate the overall surface with an accurate shape with 10–20 μm RMS error from the spin-cast glass blank [135,136].

Figure 9



Hexagonal mirror segment from the E-ELT being ground on the Cranfield BoX ultra-precision machine. Image credit: P. Comley. Reprinted from *CIRP Ann.* 60, Comley *et al.*, “Grinding metre scale mirror segments for the E-ELT ground based telescope,” 379–382, copyright 2011, with permission from Elsevier. [124].

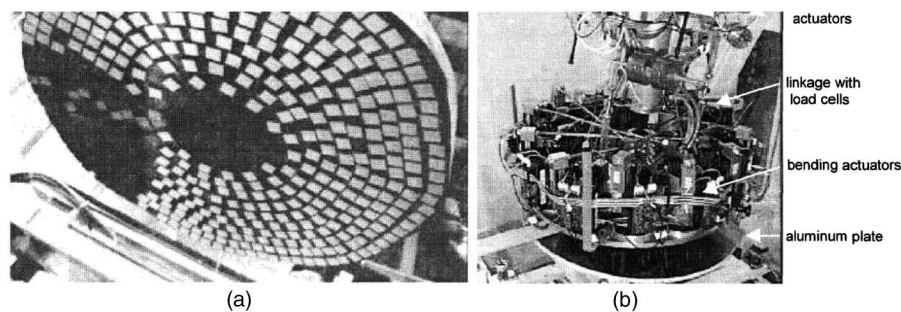
From the generating machine, the mirror is then ground and polished using the 1.2 m stressed lap and various size RC laps to achieve a high-quality surface across the 8.4 m aperture.

3.2b. Secondary Mirror Surfaces

While the primary mirror of telescopes determines a significant amount of the top-level specifications and performance, secondary mirrors are another critical component of the telescope. Most modern telescopes use a convex secondary mirror in a Cassegrain [137] or Ritchey–Chretien [138] configuration in contrast to the concave secondary of a Gregorian [139]. The choice to use such a convex secondary in this design form reduces the telescope length and aberrations, but requires unique fabrication techniques compared to the concave primary mirrors. The blanks used as substrates for the secondary mirrors are of similar materials and need to be light-weighted as much as possible to avoid a large cantilever effect when held in the telescope structure, for instance, during the on-ground system level testing phase. For primary mirrors of the 4–8 m class, secondary diameters range from 0.5–2 m, which vary depending on the system focal ratio (f-number) [140]. Typically, the secondary surfaces have 10–100 μm PV aspheric departure from their base RoC, which requires a separate step in the grinding procedure to generate. The aspherization is carried out using small diameter tools to locally treat the surface [141] or by large flexible stressed laps that are specifically set up to generate the aspheric profile [140]. Shown in Fig. 10 are examples of a full aperture polishing lap with aluminum grinding pads (a) and a sub-aperture stressed lap (b) whose tool shape is actively controlled.

As more tools are developed and processes refined, mirror production for the next generation of space telescopes will commence. Whether the design utilizes segmented primary mirrors or monolithic structures, made from carbon fiber, stacked core, or light-weighted ZERODUR, the fabrication methods will support high-precision superpolished surfaces. Developments in our understanding of removal functions, critical structural integrity, environmental behavior, and light-weighting are important parameters for future research. Understanding the current state-of-the-art methodology and optical fabrication technology is the first step in successfully producing a space telescope that enables the science goals of the future.

Figure 10



Fabrication tools used in the manufacturing of convex aspheric secondary mirrors where the aspheric profile is generated by (a) controlling the placement of aluminum polishing pads or (b) the force in the lap. The lap in (a) is 1.7 m in diameter, while the stressed lap in (b) is 300 mm in diameter. Image credit: B. K. Smith. Reprinted with permission from Smith *et al.*, *Fabrication and Testing of Aspheres* (1999), paper FT3 [140]. Reprinted with permission from Smith *et al.*, *Proc. SPIE* **3134**, 51–61 (1997) [142].

4. TESTING IN-PROCESS OPTICAL SURFACES

Throughout the fabrication phase, metrology of the mirror being made is critical for efficient, low-cost, and ultimately accurate surface production. Without the ability to test and measure the optical surface, no mirror could be efficiently fabricated. The old adage in the optical shop states, “If you can’t test it, you can’t make it.” Therefore, developing the technology to test the next generation of space optical telescopes to the precision and accuracy that is demanded by the science goals is one of the most important steps in the process. The type of testing technology used throughout the fabrication process varies dramatically from when it has a rough ground scattering surface to a specular smooth profile. The more information about the starting surface shape that can be input into the grinding machines, the more accurately and efficiently the surface can be generated and ground. Therefore, metrology tools to measure rough surfaces with a high dynamic range are critical to keeping fabrication times and costs down. Even as the surface becomes reflective in the visible spectrum, the surface profile is constantly changing with each polishing run, which requires metrology that can accommodate a large range of shape errors, which in general have a freeform shape. Finally, as the surface converges to the desired shape, precision and accuracy are of utmost importance for the testing technology.

4.1. Full-Spectrum Metrology Requirements for Astronomical Telescopes

As telescope performance requirements become ever more precisely determined, our definitions of surface specifications that will guarantee the optical performance must also be refined and carefully controlled. Modern high-precision optical surfaces are specified using a full spectrum of requirements: low-order surface profile errors, mid-spatial frequency variations, and high-spatial frequency surface roughness, as defined in Tables 2, 4, and 6. Low-order surface errors cause a broadening of the main peak of the diffraction-limited PSF while high-spatial frequency errors redistribute the power contained in the peak to areas much further away [143]. The PSF is computed by taking the Fourier transform of the exit pupil, which for a single surface is the aperture. When we have an ideal circular aperture and no aberrations, the Airy pattern is formed [47], but given errors on the surface in the mid-spatial frequency regime, the sidelobes of the Airy pattern become more pronounced. Shown in Fig. 11 is an example of the loss in PSF quality when mid-spatial frequency errors are present in an optical system [91]. To prevent these types of errors, a surface specification across the full spatial frequency spectrum is defined. The three main spatial frequency regimes can be combined together to create a PSD [91,92] or structure function [93,94] that describes the magnitude of the surface errors as a function of spatial frequency. Typically, at the high-spatial frequencies, the surface micro-roughness is determined from the random statistical processes of polishing while the low- to mid-spatial frequency regime is dominated by tool and machine specific figuring errors. Tables 2, 4, and 6 detail the optical surface requirements of the next-generation telescope mirrors, which serve as a requirement on precision and spatial sampling resolution of the metrology tools.

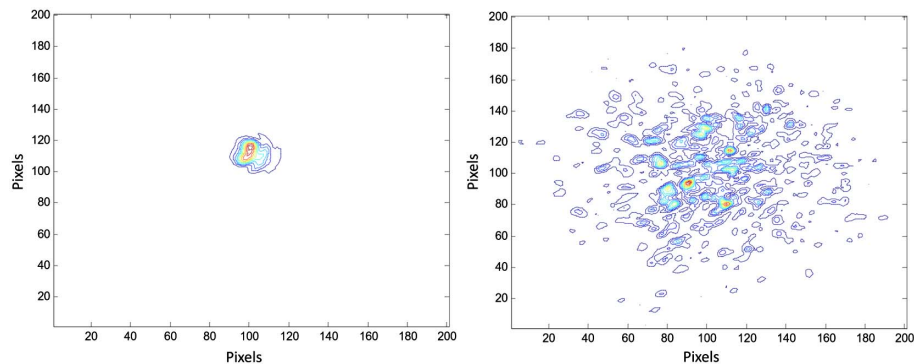
4.2. Rough Generation Stage: Measuring and Controlling the Global Shape

Defining the overall surface shape (low-order) mostly takes place during the generating and grinding stages in the manufacturing process. These processes remove material from the surface rapidly but produce a rough surface, which cannot be measured using typical optical metrology tools that have been developed for final acceptance checks. Given the requirements that the metrology tools need to measure the low-order shape of a roughly ground surface, new metrology methods have been developed. One such test employs laser trackers and distance measuring interferometers (DMIs), which has been successfully implemented in the metrology of the GMT

primary mirror segments [144,145]. The system operates by collecting roughly 200 point samples with 0.5 m spacing across the aperture of the mirror generating a point-cloud of data describing the optic. To sample the surface heights, a spherically mounted retroreflector (SMR) is used as a target for the DMI and moved across the surface in 3D space. Because the SMR is used as the target, the surface quality does not affect the measurement quality, so this method can be directly used in generation and loose abrasive grinding. Surface heights can be measured with an accuracy of $<1 \mu\text{m}$ RMS by supplementing the laser tracker with additional references and calibration of the systematic errors. Another point-sampling method to determine the shape of a ground surface is using a three-point spherometer mounted on a swing-arm profilometer [146]. In this process, the spherometer is moved in increments along a radius away from the center of the part and the part is rotated beneath the spherometer to generate the 3D surface information. Measurement accuracies of $16 \mu\text{m}$ on a 4 m class surface with a radius of curvature of 14.6 m were achieved.

The previous methods can measure the surface of the optic when it is in any stage of generation, but both have limited sampling because of the implementation. A method to obtain a more detailed surface profile has been implemented for surfaces further along in the generation stage when their surface roughness is $<10 \mu\text{m}$ RMS. This method is an IR deflectometry system and can produce height maps with much higher spatial resolution than other grinding stage metrology methods while achieving around $1 \mu\text{m}$ level accuracy [147]. The principle of deflectometry, a reverse Hartmann test, uses an optical source and an imaging camera to measure local surface slopes across the mirror aperture. Deflectometry is a non-null test method that achieves a high dynamic range. In the case of IR deflectometry, the source emits in the long-wave infrared (e.g., $10 \mu\text{m}$ wavelength), such as a long metal wire that is heated. By knowing the wire location in 2D, and measuring with the IR camera how the reflected image of the wire changes as the wire is translated in two perpendicular directions, the surface slope is calculated by triangulation. An integration step is then required to reconstruct the surface height information from the slope data. A schematic of a particular IR deflectometry setup used to measure large optical surfaces is shown in Fig. 12.

Figure 11



Autocollimation measurements of two identically specified optical systems using typical low- and high-spatial frequency (figure and finish, respectively) metrics, where the system on the left has a much smaller spot due to fewer mid-spatial frequency errors. Note that the exposure time for the image on the right is 50 times longer than the image on the left. This means mid-spatial frequency errors can also increase measurement time, because the system is not as efficient. Image credit: R. E. Parks. Reprinted with permission from Parks, Proc. SPIE **7071**, 707109 (2008) [91].

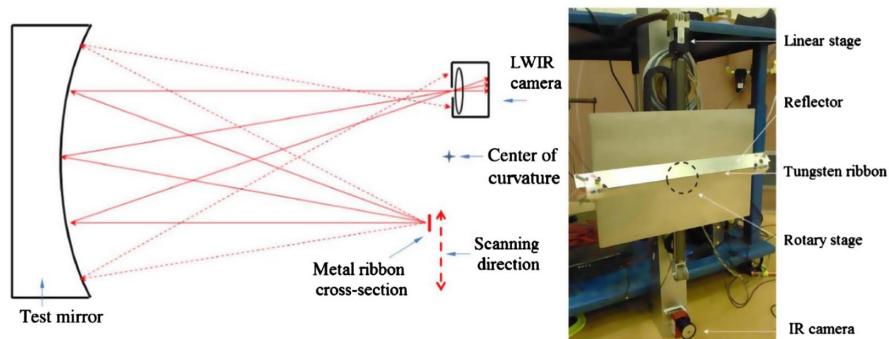
Infrared deflectometry was used with much success on the 4.2 m DKIST during the grinding stage where loose abrasives as large as 25 μm were used. This metrology tool guided the fabrication from 25 to 12 μm loose abrasive grinding, which resulted in a 1 μm RMS surface [122]. After the surface reaches this level of roughness, a clear reflection is obtained by a minimal polishing-out run and other more traditional test methods may be used in conjunction with finer fabrication methods.

The JWST primary mirror segments were measured during the generation stage using a coordinate measuring machine for initial qualification, providing a spatial resolution of 0.25 mm with an accuracy of 0.3 μm [120]. As the grinding progressed to the point of obtaining a 10 μm RMS roughness, an infrared scanning Shack Hartmann system (SSHS) was employed as a full aperture test. The infrared Shack Hartmann system was developed by Tinsley under JWST funding, and operates at a wavelength of 9.3 μm [149]. A Shack Hartmann system has a high dynamic range and is able to characterize the mid- to high-spatial frequencies on the mirror substrate. The system is scanned over the surface making sub-aperture measurements, which are then stitched together to form a high-resolution surface map of the full aperture. This type of infrared system guides the grinding stage fabrication in an efficient manner, allowing for higher quality control over the final product. A sample measurement of an aluminum surface used to test the capabilities of the SSHS is shown in Fig. 13, where residual lathe turning marks are clearly visible in the x and y slope maps (a) and (b), respectively, but become dominated by the low-order shapes in the wavefront map (c). The machined aluminum surface from the lathe was too rough to obtain quality data, so the surface was ground with automotive body shop methods [149].

4.3. Polishing and Figuring Stage: Measuring and Perfecting the Surface Quality

Final figuring of the surface through polishing occurs after the surface shape is generated and the majority of the removal is completed through grinding. In this stage, the metrology must be accurate enough to detect the small corrections applied to the surface as it converges to the final desired shape while covering the full dynamic range as the surface is in-process. This means that a non-null metrology tool is well suited for

Figure 12

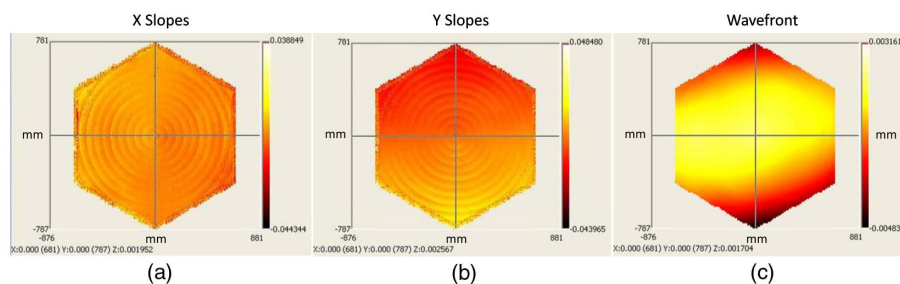


Overview of one implementation of an infrared deflectometry system used for grinding stage metrology (left) and the hardware implementation of the system (right). The long-wave infrared (LWIR) wavelength permits testing of rougher surfaces (earlier in the fabrication process), which can greatly reduce the total time of manufacturing by providing metrology data to guide the high removal processes of grinding. Image credit: T. Su. Reprinted with permission from [148]. Copyright 2013 Optical Society of America.

fabrication because it does not need to be retooled or aligned each time a polishing run is completed. The surface also has a much lower roughness, so a specular reflection in the visible spectrum is obtained, which enables a host of metrology tools previously inaccessible. Throughout the polishing phase, the low-order shape is not changed as much as the mid- to high-spatial frequencies, but it is still a critical parameter to verify and fix any residual errors from the generation and grinding stage. To measure the overall shape error, specific tests for reflective surfaces have been implemented on off-axis aspheric mirrors utilizing a scanning pentaprism technique [150]. This same tool has also been used on the primary mirror segments of the GMT to measure the surface slope (and therefore height after integration) with an accuracy of $1 \mu\text{rad}$ RMS, which is adequate to verify that the power, astigmatism, coma, and other low-order aberrations are well controlled. A similar pentaprism test has been identified as a method to control the low-order shape (conic constant, radius of curvature, etc.) on the SPICA [151]. This test complements the Hartmann test during the polishing phase, and can achieve an accuracy of 50 nm RMS.

Correcting the mid- to high-spatial frequencies is one of the most important aspects of the polishing stage, and therefore the metrology tools used must satisfy the precision and accuracy requirements and strive to remain efficient when used in the iterative fabrication process. A full aperture test that has sufficient spatial sampling to measure the mid-spatial frequencies and a large enough dynamic range to cover the ever changing surface of the in-process mirror is based on the principle of deflectometry. One deflectometry system [152] was used to guide the polishing phase of the DKIST [153] and GMT mirrors [154], resulting in a more efficient and well-controlled process. This tool is part of a larger class of visible deflectometry systems, where the source is an off-the-shelf screen, which is programmed to display sinusoidal patterns to enable a phase-shifting style measurement. Visible deflectometry is capable of making high-accuracy measurements when the system geometry is known precisely and all aspects are well calibrated. To calibrate a deflectometry system, the display and camera nonlinearities must be considered as well as the display sag due to gravity. The instrument transfer function is also important to consider when achieving the highest level of accuracy [155]. To demonstrate the accuracy of the system, a measurement of one of the GMT primary segments was made late in the polishing stage using visible deflectometry and the interferometric null test designed for the final acceptance check. The resulting surfaces from this measurement are shown in Fig. 14 where the two

Figure 13



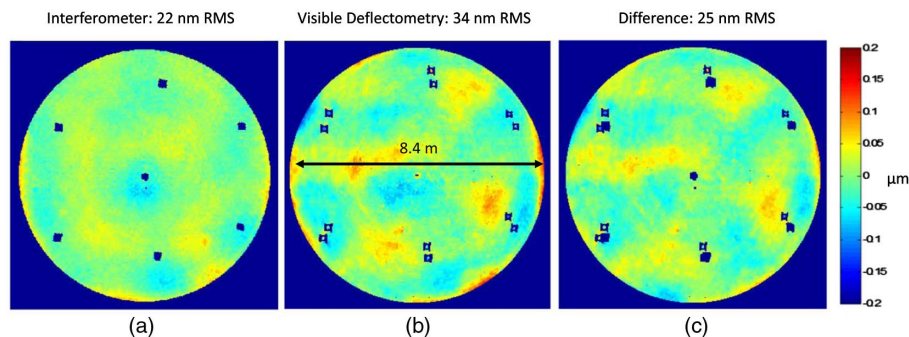
Sample measurement results of an aluminum mirror measured with the infrared scanning Shack Hartmann system (SSHS) developed for grinding phase metrology of the JWST mirrors. Shown in (a) and (b) are the x and y slopes (unitless) of the surface, respectively. These slopes are integrated to obtain the wavefront shown in (c) in units of millimeters. Image credit: C. Kiikka. Reprinted with permission from Kiikka *et al.*, Proc. SPIE 6265, 626511 (2006) [149].

datasets agree to within 25 nm RMS, which is within the uncertainty level of both the interferometric test and the deflectometry measurement. Furthermore, the high dynamic range of a visible deflectometry test was critical during polishing because the surface slopes at the edge of the mirror were initially too large for an interferometric test, but the deflectometry test was able to resolve them. This allowed the direct dwell-time-based figuring process to be applied and brought the edge errors down to the point where an interferometer could resolve the data.

Deflectometry is also capable of measuring the high-spatial frequency errors by measuring a sub-aperture of the optical surface. A portable sub-aperture deflectometry test system has been created to achieve this goal on the GMT and DKIST primary mirrors [156]. The sub-aperture deflectometry system utilizes an auxiliary lens placed close to the surface under test to change the ray paths and allow a wider range of surface curvatures to be measured. In this configuration, a portable deflectometry system readily measures convex, flat, and concave parts with the use of the lens. On the DKIST primary, the portable deflectometry tool using an auxiliary lens was able to measure surface irregularities from 10 to 1000 cycle/m over a 125 mm diameter region [122].

The typical phase-shifting deflectometry measurement relies on a temporal phase-shifting method to calculate the slopes. This cannot be applied to a dynamic surface because over the measurement duration the surface will change and corrupt the measured data. An instantaneous deflectometry system was recently developed to overcome this issue and expand the range of test cases that deflectometry systems cover [157]. The instantaneous system still uses a phase-shifting technique, but multiplexes all the required information in a single pattern, which allows a full deflectometry measurement to be made at each exposure of the camera. Due to the high dynamic range in a deflectometry system, it is now possible to measure a time varying surface with significant height variation. Applications of this system range from the measurement of a deformable mirror (DM) to the bending modes of a large optical surface due to a stimulus. Experimental evidence highlighting the capabilities of the system shows that with a unique error correction method that uses a reference surface, this technique agrees well with interferometric data.

Figure 14



Comparison of the (a) interferometric and (b) visible deflectometry data from a 8.4 m in diameter primary mirror segment of the GMT over 95% of the mirror diameter. Low-order terms related to system alignment have been removed from both datasets to highlight the mid- to high-spatial frequency agreement. Shown in (c) is the pixel-by-pixel subtraction of the two datasets where the resulting error is within the uncertainty of both measurement systems. Image credit: T. Su. Reprinted with permission from [148]. Copyright 2013 Optical Society of America.

To characterize the low- to mid-spatial frequency components of an optical surface, optical profilometry is an attractive tool. Profilometry measures the slope of the surface by observing the deflection of a narrow beam on a well-defined small area of the surface and through many scans across the surface it can reconstruct the full aperture data. Note that since the fundamental data type are slopes, they must be integrated to obtain a surface height. It has been applied to x-ray optics extensively [158], where slope measurement accuracies of better than $0.3 \mu\text{rad}$ RMS are possible [159]. Optical profilometry typically suffers from white noise at higher spatial frequencies, limiting their range of use. However, making multiple measurements and modeling noise sources are avenues to expand their utility [160].

4.4. Final Verification of Space Optics

To check if the final figuring process has converged to a desired surface, an interferometric null test comparing the real surface against the ideal (i.e., theoretically or numerically specified) mirror shape is often configured and performed using a computer-generated hologram (CGH) and/or null optics (e.g., Offner null lens). This final acceptance check is designed around a particular surface or an optical component/sub-system, such that any deviation from a perfect null result in this test precisely measures the residual shape error from the ideal design. A null test, where only a perfect match between the reference and the unit under test produces the null result has a high level of sensitivity and accuracy since there is only one single solution to create the designed null outcome achieved by matching the test wavefront and the optics under the measurement. This test differs from the deflectometry systems previously discussed due to the limited dynamic range, but increased sensitivity to deviations from ideal. A null test is performed on each optical component in the system to provide a final acceptance metric. The tests for a concave mirror (e.g., primary) differ significantly from those used on convex surfaces (e.g., secondary) because of the wavefront required to match the surface under test. Therefore, metrology tools have been developed that tackle each of these surface regimes separately.

4.4a. Null Testing of Concave Optics

For a concave surface, the null test typically employs a CGH as the null component in an interferometer because of the accuracies obtained with these measurement systems. One such system has been designed and implemented as the last step in the polishing process metrology for the GMT primary mirror segments. This test uses a fold sphere to accommodate a large portion of the astigmatism component in the test wavefront in conjunction with a CGH to generate a null [144]. The test setup is shown in Fig. 15 where the fold sphere is simultaneously measured using a separate interferometer during the principle test to account for any errors in the fold sphere. Over the 8.4 m clear aperture of the segment, 20 nm RMS residual error is achieved with the null test [101]. Alignment features can be put outside the primary CGH to make sure all the components are correctly positioned [161]. The external reference patterns are printed on the CGH at the same time as the main correction null pattern, which means they are aligned to the precision of the lithographic printing method.

4.4b. Null Testing of Convex Optics

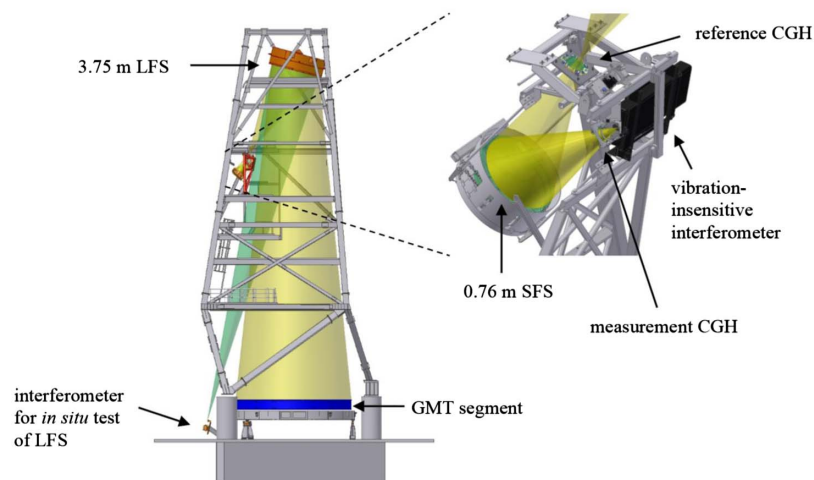
Convex metrology poses a challenging problem when designing a null test because the apertures of the null components must be at least as large as the component under test. This means that in order to create the null, one must fabricate an entirely new component with greater accuracy than what the original test optic requires. Therefore, null test methods to overcome this practical issue have been designed [162,163]. These tests once again leverage the precision of the CGH printing process to generate a null over a sub-aperture of the part. Alternatively, a variable optical null may be created

using other optics [164,165], such as Zernike plates or cylindrical lenses. Then, by moving the optic or the test system around to different regions on the surface, one can create a full aperture measurement [165,166]. However, stitching the individual sub-aperture measurements together poses a difficult challenge and can create more uncertainty than is tolerable. Sometimes, a traditional null that measures the full aperture at once is desired, and up to a 4 m diameter convex secondary has been measured using such a test [167]. This test is good for simple surfaces, but as the aspheric departure grows, a full aperture null becomes much less practical. Therefore, the sub-aperture stitching interferometry or swing-arm profilometry are becoming the most attractive options when testing modern convex secondaries [168]. When utilizing sub-aperture stitching interferometry, new data processing methods to ensure accurate data across the full aperture have been developed. Furthermore, information on the coordinates of the sub-aperture metrology tool within the coordinate frame are required to compensate for the motion of the system. Shown in Fig. 16 is an example of such a custom sub-aperture stitching tool (a) to test a 1 m class convex aspheric mirror, and the sub-aperture sampling pattern used to ensure sufficient overlap between data. In this configuration, the CGH was designed to compensate for a majority of the surface departure as the local surface changes with each sub-aperture.

4.4c. As-Flown Characterization

In the case of space optics, the final verification must be made in the zero-gravity space-thermal environment experienced on-orbit. This implies cryogenic cooling of the mirrors, and testing in a support structure that minimizes or removes the effects of gravity deformation. These requirements on the test environment place significant constraints on the test setup, but ensure that the performance of the telescope will match the expected. Large cryogenic chambers are used with liquid helium to cool

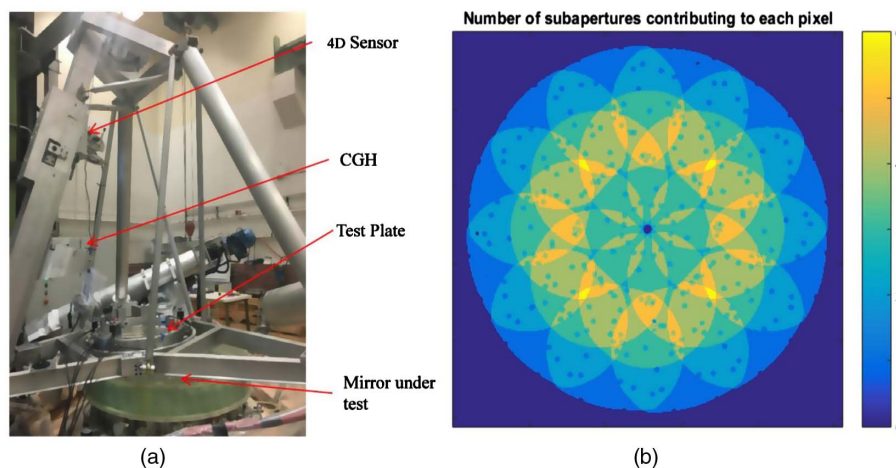
Figure 15



Computer model of the principal CGH test for the GMT off-axis segments shown in the 28 m tall test tower (left). Shown to the right is the null measurement CGH and small fold sphere (SFS). The reference CGH is inserted during alignment of the test system but removed during the actual test. The yellow cones show the light path of the principle optical test, while the green cone is the path for the simultaneous measurement of the large fold sphere (LFS). Such a null test utilizing a CGH forms the final acceptance test for the GMT mirror segments due to the high accuracy of the nulling components. Image credit: H. M. Martin. Reprinted with permission from Martin *et al.*, Proc. SPIE **8450**, 84502D (2012) [101].

the mirrors to the operational specification (e.g., JWST is at 30 K, Spitzer was at 4 K, ASTRO-F was at 9 K [169]). To eliminate the effects of gravity, measurements can be made at various rotations of the mirror, removing the effects of gravitational sag from the measured surface [170]. Optical testing of the JWST mirror segments took place at Marshall Space Flight Center's (MSFC) X-ray Cryogenic Facility [171] where a classic interferometric center of curvature test with a CGH null optic was employed [172]. The interferometer and CGH sit outside the cryo-chamber in ambient atmosphere, while the light propagates through a window into the chamber. Six segments were mounted together but tested individually. They were placed in the chamber as a unit in order to reduce testing time since cooling the chamber is very time intensive [173]. The cryogenic testing involved measuring the surface of each segment at a range of temperatures: 25 K, 32 K, 45 K, 59 K, and ambient. Data from the cryogenic tests was used to provide a final hit-map for the figuring of the mirrors before they were coated and ready for another round of final cryogenic acceptance tests.

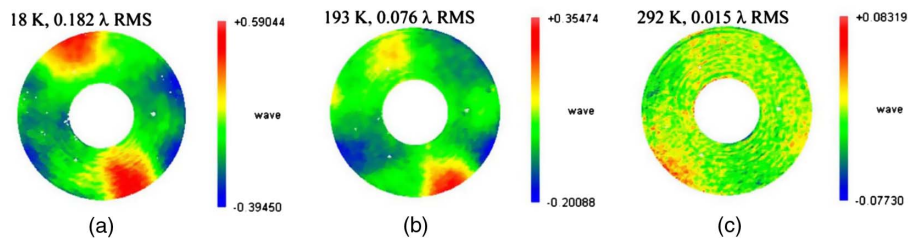
Due to the high thermal stability and thermal conductivity, SiC is used often in cryogenic conditions, such as those found on space telescopes. The planned SPICA mission will operate at 6 K, and therefore the mirrors made from SiC will need to be tested at cryogenic temperatures [174]. As a test case for this future mission, an 0.8 m mirror was tested at 18 K in the liquid helium chamber at JAXA. Similar to the JWST cryogenic tests, an interferometer was placed outside the cryogenic chamber and measured the surface during cool down and warm up. The test results showed about 110 nm RMS change at 18 K, with no significant residual deformation after warming back up. Shown in Fig. 17 are data of the mirror as it is warming up from 18 K to ambient. The ambient surface shape has been subtracted from each of these data and a measurement error of 0.01λ RMS (HeNe: $\lambda = 632.8$ nm) is reported. Efforts to predict the cryogenic performance of a mirror are in development since if an accurate model can be made and verified, significant time and money may be saved during future mission

Figure 16

Sub-aperture stitching using interferometry is a technology to measure aspheric convex mirrors, which is necessary for the next generation of space telescopes. Shown in (a) is a custom hardware setup to measure a 1 m class convex aspheric mirror and (b) the sampling pattern generated to provide sufficient overlap between data. Note that the 4D sensor is a commercial product by 4D Technology. Image credit: C. J. Oh. Reprinted with permission from Oh *et al.*, Proc. SPIE **9912**, 99120R (2016) [168].

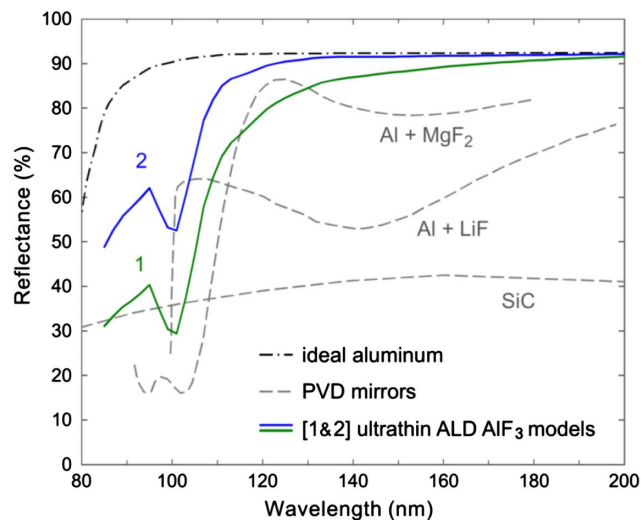
fabrication procedures [175–177]. With an accurate model for how the surface will deform in cryogenic temperatures, fabrication in ambient temperatures can yield a result that is closer to the desired surface shape. Current models for SiC show that an accuracy of 50 nm can be obtained with these models under specific conditions and well-known material properties.

Figure 17



Surface maps measured using a Fizeau interferometer of an 0.8 m diameter SiC mirror as it warms up from cryogenic temperatures: (a) 18 K, (b) 193 K, and (c) 292 K. Note that an ambient surface map has been subtracted from the datasets, showing the change due to temperature. The height data is also not plotted on the same scale and is given in units of HeNe wavelengths (632.8 nm). Measurements of the mirror surfaces in the environmental conditions of space (cryogenic temperatures) are critical to ensuring their performance. Image credit: H. Kaneda. Reprinted with permission from [174]. Copyright 2010 Optical Society of America.

Figure 18



Modeled performance of aluminum-coated mirrors with a layer of protective coating added immediately afterwards. Traditional methods are physical vapor deposition (PVD) of MgF_2 , LiF , or SiC [182]. The ultrathin atomic layer deposition (ALD) technique has been developed to coat the surfaces with AlF_3 and achieve good performance, which depends on the coating thickness. Curve 1 (green) is the result of a 3 nm layer of AlF_3 on top of a 0.3 nm thick interfacial layer of Al oxide, while curve 2 (blue) is from a 2 nm layer of AlF_3 assuming no oxide layer. Image credit: J. J. Hennessy. Reprinted with permission from Hennessy *et al.*, *J. Astron. Telesc. Instrum. Syst.* **2**, 041206 (2016) [183].

4.5. Optical Coating

After the final figuring step and verification that the optical surface meets the specifications, it is sent off to be coated with a reflective material whose reflectivity, mechanical, chemical, and thermal properties have been engineered for the particular application. The coating procedure for the next generation of space optical telescopes has the potential to open new avenues of science measurement by improving light efficiency, expanding the wavelength bands to the extreme ultraviolet [178], or even improving cryogenic performance [179]. The future UVOIR mirrors are typically coated with high reflectance Al using conventional evaporation and advanced atomic layer deposition techniques [180]. The far-UV (FUV) spectrum is most difficult to achieve a high reflectance, but offers a wealth of science data. Aluminum has been the standard choice for UVOIR mirrors since its high intrinsic reflectivity ($R > 80\%$) from 90 to 2000 nm offers good broadband performance. However, Al oxidizes quickly and degrades UV reflectivity, so the process must take place quickly in low vacuum conditions. To prevent optical degradation after the coating process, either by mechanical or chemical means, a protective layer of highly transmissive material is added on top. These are typically metal fluorides like MgF_2 , LiF, or AlF_3 [181]. Shown in Fig. 18 is the modeled reflectivity of a variety of material coatings compared to bare aluminum. These predictions are based in experimental data and demonstrate that AlF_3 has good reflectance in the FUV and even extends the cutoff wavelength over traditional PVD techniques [183]. Further experimental work has demonstrated the scalability of this approach and its environmental stability [184] through incorporating an atomic layer etching procedure [185].

Optical coating of x-ray mirrors is essential to achieve high reflectivity for high-energy photons, which is accomplished with high z metals, such as gold, platinum, and iridium. The quality of the coating also plays a significant role in optical performance since the reflectivity at grazing angle of incidence is very sensitive to changes in surface properties. The technical requirements for mirror coatings in the soft x-ray photon energy band are high reflectivity in double reflection, no surface deformations introduced, efficient coating procedure, and no degradation during storage and in the space environment. Current work to achieve these goals for future x-ray telescopes are in low-stress iridium for slumped glass substrates [186], and bilayer Ir/ B_4C for silicon pore optics [187]. Both processes are undergoing optimization to achieve the requirements for the next generation of x-ray telescopes. For hard x-rays above 10 keV, multilayer coatings of Pt/C or W/Si with nanometer thicknesses to enhance the Bragg reflectivity is accomplished with tuned spacing of layer pairs.

5. COMPONENT AND INSTRUMENT ALIGNMENT OF OPTICAL AND MECHANICAL SYSTEMS

After fabricating the optical components of the telescope they must be aligned together to produce a system that is able to make the measurements required by the system level performance. Errors in the alignment create aberrations in the optical system that degrade the performance and therefore inhibit the science. There are unique aberrations that are the product of misalignment for a given combination of optics, which can be understood through numerical simulations using ray-tracing software, or nodal aberration theory (NAT) [188]. The general class of two-mirror astronomical telescopes is well described by NAT and therefore the theory is beneficial for understanding and developing a correction method for misalignments [189]. As the mirror systems become more complex, determining the exact component misalignments for a given aberration becomes more difficult, but a handful of three-mirror anastigmatic telescopes can be successfully understood using NAT

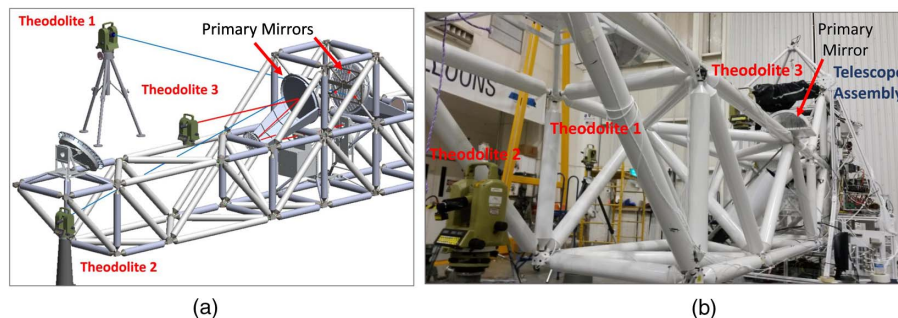
[190]. In practice, using NAT to perform an alignment generally requires multiple iterations of measuring the aberrations in the FOV of the telescope and recalculating the misalignments [191]. Understanding the misalignments of the optical system and how they affect optical performance is critical to achieving a high-quality science instrument. Each telescope poses its own unique alignment challenges, whether it is a monolithic structure or segmented assembly, and therefore tools to accomplish these tasks efficiently and accurately are continuously being developed.

5.1. Optical System Alignment

Alignment plans for all astronomical telescopes are critical parameters to establish in advance such that there is a clear method to achieve the desired system level optical performance [192]. Usually, this plan puts a tolerance on each optical component's location in 3D space with respect to a well-defined and measurable reference. One may use theoretical predictions of how the telescope behaves given a misalignment [193], but this requires measurement of the imaging performance to provide input into the alignment model, which is not always feasible for space optical systems. The alignment model also has to account for the induced stress in components when using active control of the optical surfaces to correct for low-order misalignments [194]. Too much force applied to the optical components can cause outright failure if the force creates stresses that exceed the fracture stress of the material. Even if the induced stresses do not exceed the fracture stress of the material, over time the stresses can create structural defects leading to a failure. Stresses in transmissive optical components also induce a birefringence that creates a polarization dependency and may degrade image quality. Not only do misalignments cause imaging performance degradation, but they also create errors in the pupils of an optical system. For certain applications, such as large deployable space telescopes, pupil alignment is critical for the science goals and necessitates careful considerations [195].

Depending on the sensitivity of the system to misalignments, many different strategies for aligning the components exist. At the most basic level, the alignment is completely determined by the mechanical mounting structure of the telescope. While

Figure 19

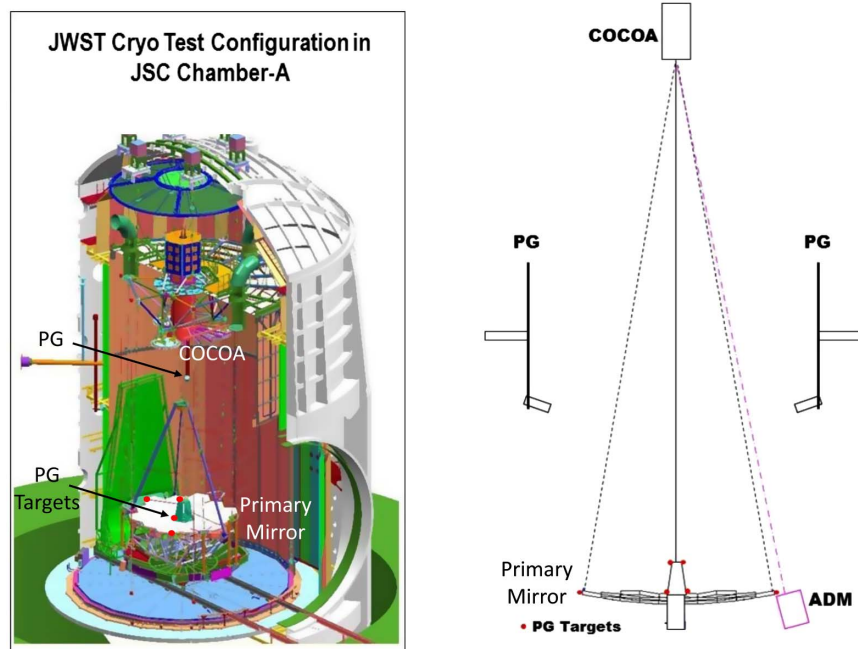


Theodolites provide an accurate method of aligning the angular geometry of the telescope, as demonstrated in the Balloon Experimental Twin Telescope for Infrared Interferometry. Shown in (a) is a model of the system that was realized (b). Each theodolite performs an angular measurement of a mission critical component, building up the full system alignment. Image credit: A. Dhabal. Reprinted with permission from Dhabal *et al.*, *J. Astron. Telesc. Instrum. Syst.* **3**, 024002 (2017) [196].

this is simple to implement, it is rarely sufficient, and therefore a measurement of the component locations must be made and the errors compensated for using actuators. To measure the location of the optical elements, laser trackers and theodolites are very attractive options because they are able to measure a wide variety of errors in a large volume with high accuracy. For instance, a commercially available laser tracker system provides $\sim 15 \mu\text{m}$ accuracy for a 2 m measurement distance case, and covers more than a 100 m diameter spherical working volume. As the accuracies of these systems have increased, so has their popularity in alignment plans. The Balloon Experimental Twin Telescope for Infrared Interferometry incorporates these alignment tools in their plan and has shown that arcminute level pointing accuracy is possible in a complex system [196]. Shown in Fig. 19 are (a) the model of the angular alignment of the telescope assembly and (b) the realization of the model. Theodolite 1 points along the two lower tooling holes behind the primary mirror, theodolite 2 points toward the normal of the primary mirror's flat outside edge, and theodolite 3 is pointing along the principle axis of the primary mirror used to align the secondary and tertiary mirrors. Note that theodolites 1 and 2 generate the coordinate system for theodolite 3.

The JWST creates a unique alignment challenge since the primary mirror is segmented but the secondary must still be aligned to the parent primary independent of any of the segment misalignments. Using multiple field point wavefront measurements, an

Figure 20



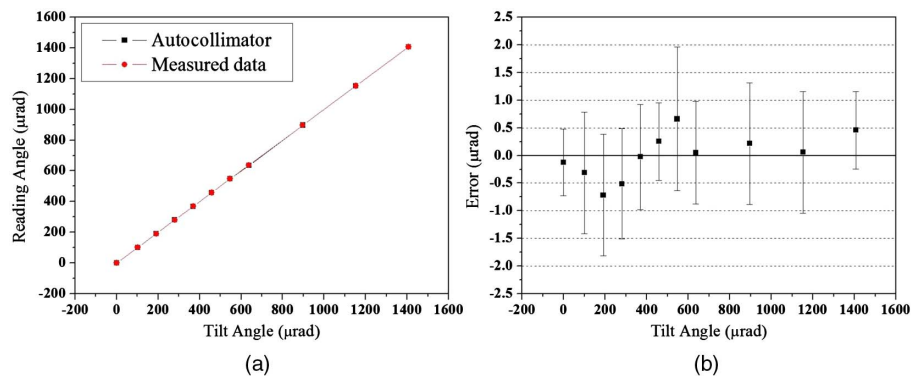
JWST cryogenic test configuration shown in the cryo-chamber (left) at Johnson Space Center (JSC) and the optical configuration of the coarse and fine mirror alignment systems (right). The photogrammetry (PG) system is used as a global coarse alignment for the outer primary mirror (PM) segments and aft optical subsystem (AOS), while the center-of-curvature optical assembly (COCOA) with help from the absolute distance meter (ADM) assembly is used as a final phase measurement. The red dots shown are locations of the PG targets, which are needed to perform the alignment with this tool. Image credit: J. Hadaway. Reprinted with permission from Hadaway *et al.*, Proc. SPIE **9904**, 99044E (2016) [201].

alignment plan for the secondary mirror of the JWST has been developed and shown in simulations to be able to account for field-dependent astigmatism and focal plane tilt due to the secondary mirror misalignments [197]. A set of linear equations describe the multifield wavefront errors that result from a misaligned secondary, which can be inverted to provide a correction for the secondary mirror position.

5.2. Segmented Mirror Alignment

Segmented primary mirrors are an attractive option for the next generation of space optical telescopes because of their compactness during launch, ease of segment production, and scalability. However, aligning each segment to form a larger optical surface becomes a necessary challenge. The alignment is called co-phasing because the surface is not strictly continuous; there are small gaps between each segment for mechanical reasons, but each segment must sample the parent surface at exactly the correct location and orientation. Thus, the wavefront reflected by the primary has no phase discontinuities between each of the segments, which will degrade the image quality. To co-phase a segmented mirror, interferometric methods can be used [198,199]. However, one challenge in this alignment is transitioning from a coarse alignment to a state where the higher accuracy metrology tools can take over for final adjustment. The ground-based test co-phasing plan for the JWST uses photogrammetry (PG) cameras for coarse alignment and then a multiwavelength interferometer completes the fine piston and tilt adjustments of the mirror segments [200]. This procedure has been validated in cryogenic conditions using the pathfinder telescope in 2015. Shown in Fig. 20 is a model of the test setup and a schematic diagram. The PG systems start with a coarse error of the order of millimeters, which is brought down to a final 10 nm RMS by the interferometer [201]. On orbit, no PG cameras will be present to aid in the coarse alignment and co-phasing of the mirrors. Therefore, an iterative approach over several months will be used to establish the initial on-orbit alignments. Precise optical alignment will be achieved and maintained using wavefront sensing imagery from the science instruments [202].

Figure 21



Angular alignment of mirrors is critical to ensure the success of the segmented primary mirror designs of future telescopes. Shown in (a) are angular measurement results comparing a proposed method based on sheared Fourier analysis (red) to an autocollimator (black), which is taken as the reference. In this experiment, a flat mirror was tilted using a piezo electric motor and measured with both systems independently. The errors between each measured data point are given in (b), where the error bars represent the standard deviation of 30 data. Image credit: H. Choi. Reprinted with permission from [203]. Copyright 2017 Optical Society of America.

Developments to improve the coarse alignment of segmented mirrors are on-going and will eventually provide a more efficient and accurate method of positioning the segments. One multisegment alignment technology utilizes a sheared Fourier analysis to obtain the tip/tilt of many mirror segments over a wide dynamic range [203]. This multisegment alignment system uses a similar setup to the deflectometry system used during fabrication, where a 2D sinusoidal pattern is displayed on a screen and the pattern is captured by a camera in reflection from the segments under test. By collecting sequential images and computing a Fourier transform of the difference in the initial image to the current image, the tip and tilt alignment of each segment is determined accurately and in real time. The multisegment alignment system has been demonstrated using a set of seven flat hexagonal mirror segments, where the precision of orientation was $2 \mu\text{rad}$ (0.41 arcsec) over a range of 1.4 mrad. Shown in Fig. 21 are measured data from the case of a single flat mirror which was also measured using an autocollimator as a reference. With the autocollimator, higher accuracy is obtained, but it cannot measure multiple segments simultaneously.

Other methods to do fine co-phasing and alignment of the segments are also being developed. One example uses a Zernike phase-contrast plate to expand the dynamic range of a wavefront sensor, which can provide a final phased pupil with an RMS error of less than $\lambda/80$ [204], where λ is wavelength. This technique also can work alongside a traditional Shack–Hartmann wavefront sensor, which provides a larger dynamic range than the Zernike plate and wavefront sensor.

6. OPTICAL SYSTEM PERFORMANCE: END-TO-END TESTING

After an optical system has been aligned, a final test of the end-to-end system performance is the final check before the system can be accepted for use. These tests simulate the operating conditions of the optical system as closely as possible.

6.1. Telescope Testing

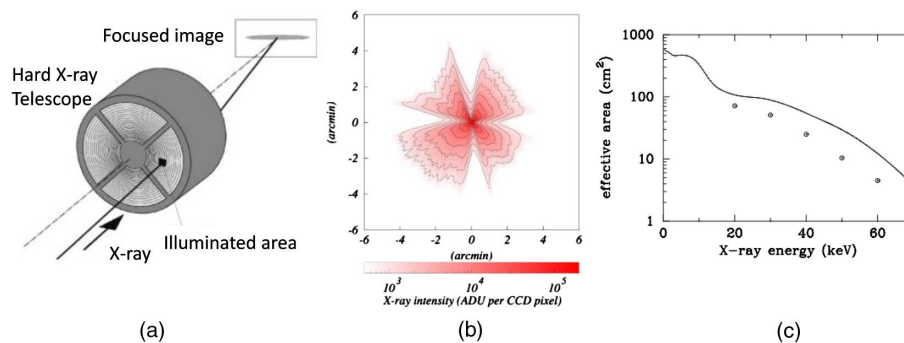
Pre-flight calibration is essential to reconstruct original images and spectra of celestial objects from observed data, especially for x-ray optics. The energy response of an x-ray telescope is sensitive to the surface material and roughness because the wavelength of x-ray is so short that small surface roughness causes significant scattering. Therefore, measurements of the flight mirror's reflectivity and scattering need to be completed [108,205,206]. The complex dependence of reflectivity has to be confirmed with enough angular and spectral resolution for sophisticated coatings. An x-ray star is simulated in test facilities by using a collimated sub-aperture beam scanned in two dimensions. The telescopes and the focal plane detectors are synchronously moved as if a pencil x-ray beam scans over the telescope. An alternative way is through a semi-parallel beam produced by a diverging beam from a point source located 200 m or farther away. The response matrices of the telescopes have to be constructed based on the x-ray measurements with certain x-ray energies and incident angles, which will be performed with a strong and monochromatic x-ray beam of a synchrotron orbital radiation (SOR) facility [207,208]. Shown in Fig. 22 is an example of the type of data that is collected at SORs, measuring the optical performance of the telescopes. The models of the surface characteristics are tuned to reproduce the measured data which has a known x-ray energy and incident angle. Final adjustment is performed with the test observation of well-known x-ray stars in the orbital environment.

The JWST team has developed very extensive tests to create the cryogenic environment that the telescope will experience when used on orbit [209]. The system level tests are first completed on the science instrument assembly [210] and finally planned

as a full system [211], where multiple test methods will be implemented to reduce the risk during the test. However, due to the very large aperture of the telescope and gravity deformation of the light-weight mirrors, a full-scale test of the system is not possible. Therefore, verification of the system performance is based on sub-system testing and high-fidelity modeling. To accomplish the scaled system test, which is carried out at NASA Johnson Space Center, a source will be placed at the intermediate telescope focus, illuminating the secondary and primary mirrors, retroreflected back through the full telescope and into the science instruments. This allows a characterization of the imaging performance of the telescope in an end-to-end fashion. Due to a high-vibration environment, a Hartmann test has also been designed to work in parallel with the planned system test. The Hartmann test is robust against dynamic jitter in the measurement because a large number of averages is possible. Along with the optical system tests of the JWST, measurements of the mechanical structure that supports the optical components are also carried out [212]. This test characterizes the impulse response function of the mechanical assembly to minimize and understand the optical performance degradation due to mechanical vibrations and even failures.

The SPICA also has undergone extensive system testing and planning for their future launch. Part of the planned system tests involve cryogenic testing at temperatures below 10 K [213,214]. The total wavefront error of the telescope will be measured using an interferometer in autocollimation, similar to the cryogenic tests implemented on the JWST. To yield a full aperture measurement, a sub-aperture test and stitching will be implemented since the autocollimating flats (ACFs) have a diameter much smaller than the telescope aperture. To sample the aperture, the ACFs are rotated about the optical axis of the telescope and therefore sample the aperture as a function of angle. Shown in Fig. 23 is the cryogenic chamber that the telescope will be tested

Figure 22



Test results of the hard x-ray telescope on the InFOC μ S experiment made at the Super Photon ring-8 GeV (SPring-8) beamline BL20B2 synchrotron facility. A cylindrically shaped x-ray telescope consisting of multinested mirror shells is illuminated by a monochromatic pencil beam from a synchrotron orbital radiation (SOR) facility. A focused x-ray beam is measured by an imaging detector on the focal plane, as is shown in (a). X-ray images are accumulated while the pencil beam scans across the entire telescope aperture, as shown with the contour map in (b), where the color represents analog to digital units (ADU). Four leaves are created by the four boundaries of the telescope quadrants seen in (a). Shown in (c) is the measured effective area of the telescope plotted as circles compared to the model calculation (solid line). The deviation from the model can be explained by the photon losses due to figure errors in the mirror shape. Image credit: Y. Ogasaka. Reprinted with permission from [207]. Copyright 2008 The Japanese Society of Applied Physics.

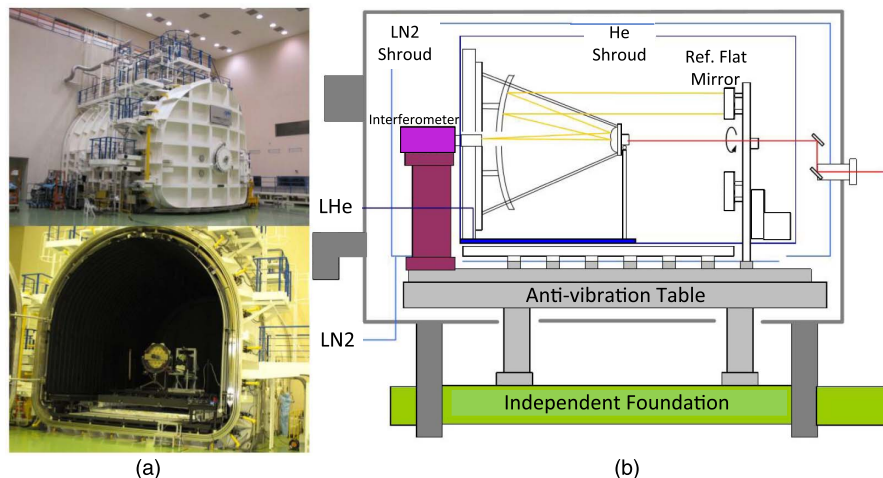
in, and a schematic of the test. The sub-aperture test methodology has been verified through an experimental study where the main purpose was to verify the cryogenic optical performance of the mirror substrate material [215]. A simulation of the sub-aperture test has also been carried out and provides justification for this methodology.

6.2. Active Correction

Active optics within the observatory can simplify the manufacturing process of the primary mirror as well as the telescope integration and mechanical design, mitigating development risks, minimizing costs and enabling large-aperture optical mission performances. The use of active optics in the system allows rigid-body motion of the mirrors for optical positioning and alignment, correcting shape errors of the mirrors (manufacturing, gravity release, moisture desorption, etc.), and the temporal variations due to thermoelastic effects. Active optics are articulated around the following three key building block elements: corrective element (e.g., deformable mirror, tip/tilt mirror), wavefront sensing system, and algorithms for correction calculation (based on wavefront sensing results) and control of the correction element. The active correction system and its end-to-end performance must also be tested dynamically and this becomes an important part of the final testing campaign.

In Europe, both the ESA [216] and the Centre National d'Etudes Spatiales (CNES) [217] are currently envisioning the use of active optics for potential future large optical missions. An example of the type of active optics are deformable mirrors (DMs), such as those tested by a team at CNES [217], the National University of Ireland Galway (NUIG) and Fraunhofer IOF [218], TNO Technical Sciences [219], and Muenster University of Applied Sciences [220], among others. Placing the deformable mirror in a conjugate plane of the primary mirror reduces its size and facilitates its manufacturability and testing. The distribution of actuators within the active optic impacts its ability to correct the wavefront errors, where a smaller number of actuators is desirable. For instance, in the case of the active correction loop developed by NUIG

Figure 23

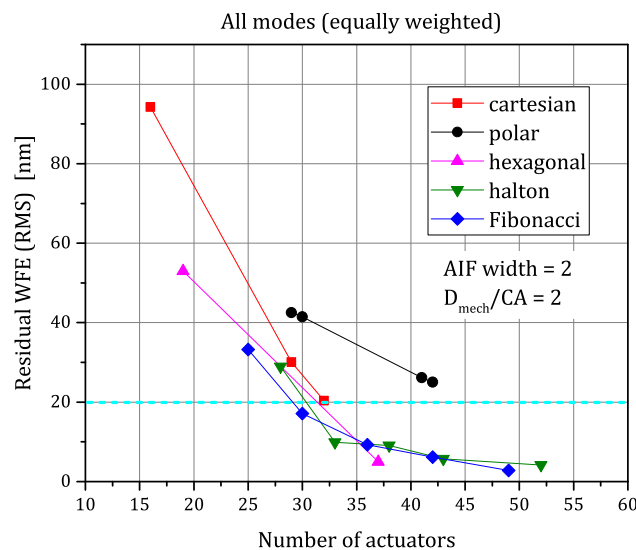


SPICA requires unique metrology for the system level test due to the large-aperture and cryogenic environment. (a) The 6 m cryogenic chamber that will be used as the system level test for SPICA and (b) a schematic diagram of the optical test that utilizes a sub-aperture measurement of the system in an interferometric autocollimation test. Image credit: H. Kaneda. Reprinted with permission from Kaneda *et al.*, Proc. SPIE 7731, 77310V (2010) [213].

based on a DM designed by IOF, a Fibonacci distribution across the pupil, or mirror surface, was initially chosen after comparing it to alternative distributions for large UV-to-IR telescope applications [221]. Shown in Fig. 24 are the results of analytical simulations showing the residual RMS error when reconstructing the sum of a specified set of Zernike modes for the various actuator distributions and number of actuators. Given a more efficient actuation method, a higher number of actuators may be implemented, allowing for a better residual wavefront error. Another DM developed by TNO for space applications using 427 electromagnetic actuators has shown promise to achieve large stroke, low non-linearity and hysteresis, and low power consumption [219]. Another style of deformable mirror (developed by the Muenster University of Applied Sciences) features a unimorph mirror surface, which is actuated using a piezo disc sandwiched between two metallic electrodes [220]. The bottom electrode is structured into a 44-electrode keystone pattern optimized for producing low-order Zernike modes. Another example of an implementation of a piezo-based monomorph DM at CILAS [222] is currently reaching qualification for space.

Alternatively, the deformable component can be the primary mirror itself. On most large-aperture ground-based telescopes, the primary mirror is actively controlled to compensate for any large-scale and slowly varying wavefront errors, avoiding adverse pupil imaging aberration effects inherent to DMs located in a pupil conjugate plane. To overcome this limitation, the Telescope to Observe Planetary Systems proposed an active thermal figure control concept [223]. This utilizes heating and cooling devices distributed within the cells of the light-weighted mirror. Finite element models have

Figure 24



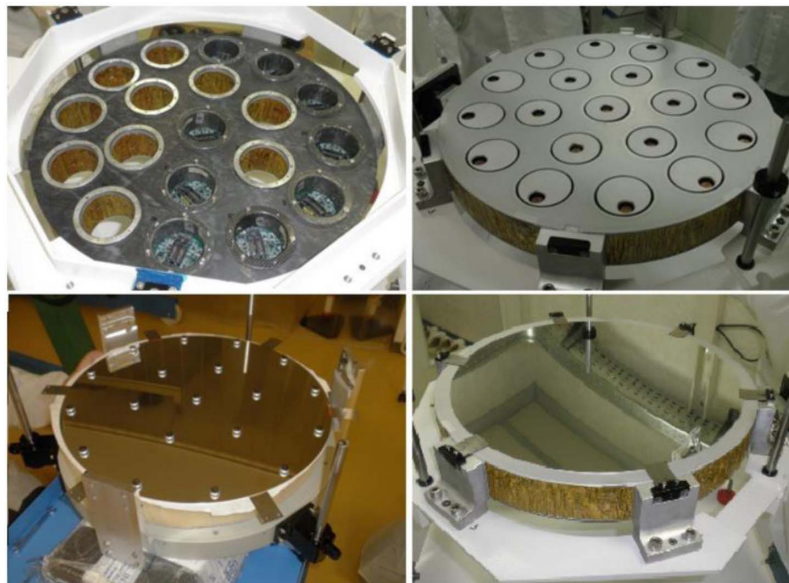
Analytic simulation results showing the reconstruction performance of deformable mirrors with different actuator distributions. A set of Zernike modes (Z5–29 in Noll index) is specified as the surface to reconstruct, and the residual error in this process is calculated. The lowest number of actuators that provide the specified residual RMS error (ex: dashed line at 20 nm RMS) in this scenario is the Fibonacci distribution. In this simulation all Zernike modes were weighted equally, the ratio of the mechanical extent of the DM (D_{mech}) to the clear aperture (CA) was set at 2, and the actuator influence function (AIF) is assumed to be Gaussian with a $1/e^2$ width defined as twice the distance between actuators on the grid. Image credit: M. Goy. Reprinted with permission from Goy *et al.*, Proc. SPIE **10562**, 1056233 (2017) [221].

shown that this method can correct up to N Zernike modes with better than 90% fidelity, where N is the number of cells in the honeycomb light-weight structure. Another deformable primary mirror concept, the large-aperture telescope technology (LATT) [224], uses an approach already implemented on the European Southern Observatory's Very Large Telescope deformable secondary mirror, based on a very thin glass shell controlled through contactless voice coil actuators with co-located capacitive position sensors, and adapted for space requirements (environment and light weighting) reaching an areal density of 17 kg/m^2 . Shown in Fig. 25 is the 0.42 m in diameter, demonstration prototype, active primary mirror for the LATT project. Another example of an active primary for space applications relies on a multi-layer active shell approach for a CFRP substrate, with a sheet of piezo material as the active layer [225].

Already, the first signs of active optics implementations in space projects can be found. For instance, the JWST will include active optics in order to adjust phasing of its large segmented deployable primary mirror and correct for line of sight variations [226], while the future NASA mission Wide Field Infrared Survey Telescope will include deformable mirrors in its coronagraph to correct for wavefront error instabilities in order to reach the extreme contrast required [227]. ESA initiated studies are also making the case for use of active correction loops for Space-based Astronomy [218] future large missions.

Looking further into the future, active correction can enable even more ambitious and innovative large payload architectures such as TALC [73,75], a far-infrared telescope

Figure 25



Prototype demonstrator for the active 400 mm diameter primary mirror on the LATT project, shown in multiple stages of integration and testing. The aluminum honeycomb reference body (top left) is populated with voice coils (top right), which provide the actuation forces. Magnets are attached to the non-optical side of the mirror (bottom left), which allows the optical surface to float above the backing. The mirror surface is a glass thin shell (bottom right) thinned to 1 mm thick. This prototype mirror has a spherical profile with a radius of curvature of 5 m and 19 actuators. Image credit: R. Briguglio. Reprinted with permission from Briguglio *et al.*, Proc. SPIE **9904**, 990410 (2016) [224].

with a 20 m deployable annular primary mirror consisting of ultralight identical CFRP segments (stacked on top of each other while in launch configuration) deployed within an actively controlled tensegrity truss structure [74]). Distributed over the whole spacecraft, the active correction takes place in the structure itself (adjustable ropes), in the segments (actuators for shape and position control), and in a deformable mirror located in the pupil relay. Once demonstrated for the far-infrared, this concept could pave the way for an implementation in the visible wavelength range.

6.3. Stray Light Suppression

Imaging performance is not the only system level optical characterization that is important for space optical systems. Stray light suppression will be critical for the next generation of telescopes to meet many of the sciences goals surrounding exoplanet detection requiring extremely high contrast imaging. The evolved Laser Interferometer Space Antenna system has undergone testing and characterization of their stray light suppression [228]. Their requirement for scattered light is 1×10^{-10} suppression of transmitted power into the field of view of the coherent interferometric detector. Currently, the test to experimentally verify this requirement is being designed but software models have helped constrain the required surface roughnesses to achieve the desired level of suppression [229].

7. CONCLUDING REMARKS

The next generation of optical telescopes will require further innovations across many disciplines and collaboration among many scientists and engineers. Over the course of the last decade, mission developments and science requirements have guided research in these various areas to produce amazing new results, technologies, and methods. The current state of technology to support the fabrication, testing, alignment, and performance verification of the space telescopes and their instruments is very promising and inspiring. However, further development in these areas is required to enable the optics that will be used to make paradigm-shifting scientific observations and discoveries. While improvements are still needed in these areas of technology, we should also marvel at the progress we have made and appreciate those who have put in the time and effort to make these leaps possible. Technology in the space optics fields has progressed rapidly over the course of the past decade, in which new and innovative techniques were developed to meet the growing needs of the optical community. We continue to push the limits of what is considered possible by improving accuracy, reducing costs, and producing amazingly high-quality optics. This is no trivial feat and we hope that this review article of a small sampling of the current technology has allowed you to appreciate this aspect as well.

Given the limited amount of resources and growing need for ever bigger telescopes, the development of the supporting technology is framed in the cost-saving mind set while also pushing the limits of precision and accuracy. To reduce the cost of launch, the areal density of the telescope mirrors must be reduced while simultaneously maintaining the stiffness and thermal stability properties to produce the highest-quality imaging system that survives launch conditions. Reducing fabrication time through more efficient and deterministic computer controlled grinding, polishing, and metrology will allow larger-aperture space telescopes to be launched since the available budget will go further. As metrology methods that span spatial frequency regimes become more accurate, techniques to align optical assemblies take less time, and final optical performance verification is more reliable, the cycle of development will be reduced and therefore create more cost-effective space observatory looking at the dawn of the Universe. Through these developments, the goals identified in the National Academy 2010 Decadal Report and by ESA of fundamental physics

research, the search for exoplanets, and understanding the formation of the universe are becoming a realizable achievement through the progression and development of space optics technology. The optical fabrication, testing, alignment, and as-built verification technology plays a critical role in enabling the science objectives. Without these developments, our understanding of the universe, solar system, and fundamental physics would be severely limited to Earth-bound experiments. A fundamental question to our nature as humans is, “Where did we come from and where are we going?” In order to answer such basic questions, we need extremely high-sensitivity measurements made with large-scale space-based telescopes enabled by transformative instruments. Through research and development activities in space optics technology, we will improve and expand our knowledge concerning our existence and place in the cosmos, attempting to answer questions that humans across all of time have pondered.

ACKNOWLEDGMENT

The authors would like to thank the Technology Research Initiative Fund (TRIF) Optics/Imaging Program, through the College of Optical Sciences at the University of Arizona, the Post-processing of Freeform Optics project supported by the Korea Basic Science Institute, and the Friends of Tucson Optics (FoTO) Endowed Scholarships in Optical Sciences. The authors would also like to acknowledge the II-VI Foundation Block-Gift Program for helping support general deflectometry research in the Large Optics Fabrication and Testing (LOFT) group. The authors wish to thank the individuals who contributed figures and images of their research. We greatly appreciate your contributions to the field and for allowing us to use the images in our manuscript. We also want to thank the people who contributed to the editing and reviewing of the manuscript. A special thank you goes to Matthew Bolcar who helped edit and gave feedback on the article.

REFERENCES

1. National Research Council, *New Worlds, New Horizons in Astronomy and Astrophysics* (National Academies, 2010).
2. “ESA cosmic vision,” <http://sci.esa.int/cosmic-vision/>.
3. B. Mennesson, S. Gaudi, S. Seager, K. Cahoy, S. Domagal-Goldman, L. Feinberg, O. Guyon, J. Kasdin, C. Marois, D. Mawet, M. Tamura, D. Mouillet, T. Prusti, A. Quirrenbach, T. Robinson, L. Rogers, P. Scowen, R. Somerville, K. Stapelfeldt, D. Stern, M. Still, M. Turnbull, J. Booth, A. Kiessling, G. Kuan, and K. Warfield, “The habitable exoplanet (HabEx) imaging mission: preliminary science drivers and technical requirements,” *Proc. SPIE* **9904**, 990410 (2016).
4. J. A. Crooke, A. Roberge, S. D. Domagal-Goldman, A. M. Mandell, M. R. Bolcar, N. M. Rioux, M. R. Perez, and E. C. Smith, “Status and path forward for the large ultraviolet/optical/infrared surveyor (LUVOIR) mission concept study,” *Proc. SPIE* **9904**, 990410 (2016).
5. A. R. Cooray and O. S. T. S. Team, “Origins space telescope,” in *American Astronomical Society Meeting #229* (2017), p. 405.
6. J. A. Gaskin, R. Allured, S. R. Bandler, S. Basso, M. W. Bautz, M. F. Baysinger, M. P. Biskach, T. M. Boswell, P. D. Capizzo, K.-W. Chan, M. M. Civitani, L. M. Cohen, V. Cotroneo, J. M. Davis, C. T. DeRoo, M. J. DiPirro, A. Dominguez, L. L. Fabisinski, A. D. Falcone, E. Figueroa-Feliciano, J. C. Garcia, K. E. Gelmis, R. K. Heilmann, R. C. Hopkins, T. Jackson, K. Kilaru, R. P. Kraft, T. Liu, R. S. McClelland, R. L. McEntaffer, K. S. McCarley, J. A. Mulqueen, F. Özel, G. Pareschi, P. B. Reid, R. E. Riveros, M. A. Rodriguez, J. W. Rowe, T. T. Saha, M. L. Schattenburg, A. R. Schnell, D. A. Schwartz,

- P. M. Solly, R. M. Suggs, S. G. Sutherland, D. A. Swartz, S. Troler-McKinstry, J. H. Tutt, A. Vikhlinin, J. Walker, W. Yoon, and W. W. Zhang, "Lynx mission concept status," *Proc. SPIE* **10397**, 1039713 (2017).
7. X. Barcons, D. Barret, M. Bautz, J. Bookbinder, J. Bregman, T. Dotani, K. Flanagan, R. Fraga, J. Grady, H. Kunieda, D. H. Lumn, K. Mitsuda, K. Nandra, T. Ohashi, L. Piro, N. Rando, L. Struder, T. Takahashi, T. G. Tsuru, and N. E. White, "International X-ray observatory (IXO) assessment study report for the ESA cosmic vision 2015–2025," arXiv:1102.2845 (2011).
 8. R. Petre, A. Ptak, J. Bookbinder, M. Garcia, R. Smith, M. Bautz, J. Bregman, D. Burrows, W. Cash, C. Jones-Forman, S. Murray, P. Plucinsky, B. Ramsey, R. Remillard, C. Wilson-Hodge, G. Karpati, A. Nicoletti, and P. Reid, "The NASA x-ray mission concepts study," NASA Technical Reports Server (2012).
 9. "The ATHENA X-ray observatory: community support portal," <http://www.the-athena-x-ray-observatory.eu/science.html>.
 10. D. S. Hudson, T. H. Reiprich, T. E. Clarke, and C. L. Sarazin, "X-ray detection of the proto supermassive binary black hole at the centre of Abell 400," *Astron. Astrophys.* **453**, 433–446 (2006).
 11. "3C 75 in Abell 400: Black holes determined to be bound," <http://chandra.harvard.edu/photo/2006/a400/>.
 12. M. R. Bolcar, K. Balasubramanian, J. Croke, L. Feinberg, M. Quijada, B. J. Rauscher, D. Redding, N. Rioux, S. Shaklan, H. P. Stahl, C. M. Stahle, and H. Thronson, "Technology gap assessment for a future large-aperture ultraviolet-optical-infrared space telescope," *J. Astro. Telesc. Instrum. Syst.* **2**, 041209 (2016).
 13. M. R. Bolcar, K. Balasubramanian, M. Clampin, J. Croke, L. Feinberg, M. Postman, M. Quijada, B. Rauscher, D. Redding, N. Rioux, S. Shaklan, H. P. Stahl, C. Stahle, and H. Thronson, "Technology development for the advanced technology large aperture space telescope (ATLAST) as a candidate large UV-optical-infrared (LUVOIR) surveyor," *Proc. SPIE* **9602**, 960209 (2015).
 14. D. C. Redding, L. Feinberg, M. Postman, H. P. Stahl, C. Stahle, and H. Thronson, "Beyond JWST: performance requirements for a future large UVOIR space telescope," *Proc. SPIE* **9143**, 914312 (2014).
 15. H. P. Stahl, M. Postman, and W. S. Smith, "Engineering specifications for large aperture UVO space telescopes derived from science requirements," *Proc. SPIE* **8860**, 886006 (2013).
 16. H. P. Stahl, R. Barney, J. Bauman, L. Feinberg, D. McCleese, and U. Singh, "Optical manufacturing and testing requirements identified by the NASA Science Instruments, Observatories, and Sensor Systems Technology Assessment," *Proc. SPIE* **8126**, 812603 (2011).
 17. M. J. Turner, G. Palumbo, J. Bleeker, G. Hasinger, A. Peacock, and J. Trumper, "Xeus: an X-ray observatory for the post-XMM era," in *The Next Generation of X-ray Observatories: Workshop Proceedings Leicester X-ray Astronomy Group Special Report XRA* (1997), Vol. **97**.
 18. N. Rando, O. Brunner, D. Doyle, B. Fransen, A. Heras, J. M. Lautier, M. Linder, L. Popken, and T. Nakagawa, "Assessment study of the SPICA telescope assembly," *Proc. SPIE* **7436**, 74368 (2009).
 19. J. Aird, K. Nandra, E. S. Laird, A. Georgakakis, M. L. N. Ashby, P. Barmby, A. L. Coil, J.-S. Huang, A. M. Koekemoer, C. C. Steidel, and C. N. A. Willmer, "The evolution of the hard X-ray luminosity function of AGN," *Mon. Not. R. Astron. Soc.* **401**, 2531–2551 (2010).
 20. A. Georgakakis, K. Nandra, E. S. Laird, J. Aird, and M. Trichas, "A new method for determining the sensitivity of X-ray imaging observations and the X-ray number counts," *Mon. Not. R. Astron. Soc.* **388**, 1205–1213 (2008).

21. J. A. Gaskin, M. C. Weiskopf, A. Vikhlinin, H. D. Tananbaum, S. R. Bandler, M. W. Bautz, D. N. Burrows, A. D. Falcone, F. A. Harrison, R. K. Heilmann, S. Heinz, R. C. Hopkins, C. A. Kilbourne, C. Kouveliotou, R. P. Kraft, A. V. Kravtsov, R. L. McEntaffer, P. Natarajan, S. L. O'Dell, R. Petre, Z. R. Prieskorn, A. F. Ptak, B. D. Ramsey, P. B. Reid, A. R. Schnell, D. A. Schwartz, and L. K. Townsley, "The X-ray surveyor mission: a concept study," *Proc. SPIE* **9601**, 96010J (2015).
22. J. Tueller, H. A. Krimm, T. Okajima, S. D. Barthelmy, S. M. Owens, P. J. Serlemitsos, Y. Soong, K.-W. Chan, Y. Ogasaka, R. Shibata, K. Tamura, A. Furuzawa, Y. Tawara, H. Kunieda, and K. Yamashita, "InFOC μ S hard X-ray imaging telescope," *Exp. Astron.* **20**, 121–129 (2005).
23. B. Salmaso, S. Basso, C. Brizzolari, M. Civitani, M. Ghigo, G. Pareschi, D. Spiga, G. Tagliaferri, and G. Vecchi, "Direct hot slumping of thin glass foils for future generation x-ray telescopes: current state of the art and future outlooks," *Proc. SPIE* **10563**, 105639 (2017).
24. H. Awaki, H. Kunieda, M. Ishida, H. Matsumoto, A. Furuzawa, Y. Haba, T. Hayashi, R. Iizuka, K. Ishibashi, M. Itoh, T. Kosaka, Y. Maeda, I. Mitsuishi, T. Miyazawa, H. Mori, H. Nagano, Y. Namba, Y. Ogasaka, K. Ogi, T. Okajima, S. Sugita, Y. Suzuki, K. Tamura, Y. Tawara, K. Uesugi, and S. Yamauchi, "Performance of ASTRO-H hard x-ray telescope (HXT)," *Proc. SPIE* **9905**, 99058 (2016).
25. M. J. Collon, M. Ackermann, R. Günther, G. Vacanti, M. W. Beijersbergen, M. Bavdaz, E. Wille, K. Wallace, J. Haneveld, M. O. Riekerink, A. Koelewijn, C. van Baren, P. Müller, M. Krumrey, V. Burwitz, G. Sironi, and M. Ghigo, "Aberration-free silicon pore x-ray optics," *Proc. SPIE* **8861**, 886111 (2013).
26. M. Beijersbergen, S. Kraft, R. Gunther, A. L. Mieremet, M. Collon, M. Bavdaz, D. H. Lumb, and A. J. Peacock, "Silicon pore optics: novel lightweight high-resolution x-ray optics developed for XEUS," *Proc. SPIE* **5488**, 54887 (2004).
27. M. J. Collon, R. Günther, M. Ackermann, R. Partapsing, G. Vacanti, M. W. Beijersbergen, M. Bavdaz, K. Wallace, E. Wille, M. O. Riekerink, J. Haneveld, A. Koelewijn, C. van Baren, P. Müller, M. Krumrey, M. Freyberg, A. C. Jakobsen, and F. Christensen, "Design, fabrication, and characterization of silicon pore optics for ATHENA/IXO," *Proc. SPIE* **8147**, 814710 (2011).
28. H. Collaboration, "The quiescent intracluster medium in the core of the Perseus cluster," *Nature* **535**, 117–121 (2016).
29. F. Nicastro, S. Mathur, M. Elvis, J. Drake, T. Fang, A. Fruscione, Y. Krongold, H. Marshall, R. Williams, and A. Zezas, "The mass of the missing baryons in the X-ray forest of the warm-hot intergalactic medium," *Nature* **433**, 495–498 (2005).
30. J. S. Kaastra, R. Mewe, and T. Raassen, "New results on X-ray models and atomic data," *Highlights Astron.* **13**, 648–650 (2005).
31. J. N. Bregman, "The search for the missing baryons at low redshift," *Annu. Rev. Astron. Astrophys.* **45**, 221–259 (2007).
32. F. Vazza, G. Brunetti, C. Gheller, R. Brunino, and M. Brüggén, "Massive and refined. II. The statistical properties of turbulent motions in massive galaxy clusters with high spatial resolution," *Astron. Astrophys.* **529**, A17 (2011).
33. D. A. Buote and P. J. Humphrey, *Dark Matter in Elliptical Galaxies* (Springer, 2012).
34. C. Done, M. Gierliński, and A. Kubota, "Modelling the behaviour of accretion flows in X-ray binaries," *Astron. Astrophys. Rev.* **15**, 1–66 (2007).
35. M. M. Romanova and A. K. Kulkarni, "Discovery of drifting high-frequency quasi-periodic oscillations in global simulations of magnetic boundary layers," *Mon. Not. R. Astron. Soc.* **398**, 1105–1116 (2009).

36. B. De Marco, G. Ponti, M. Cappi, M. Dadina, P. Uttley, E. M. Cackett, A. C. Fabian, and G. Miniutti, "Discovery of a relation between black hole mass and soft X-ray time lags in active galactic nuclei," *Mon. Not. R. Astron. Soc.* **431**, 2441–2452 (2013).
37. M. Dovčiak, F. Muleri, R. W. Goosmann, V. Karas, and G. Matt, "Light-bending scenario for accreting black holes in X-ray polarimetry," *Astrophys. J.* **731**, 1–15 (2011).
38. F. Marin, D. Porquet, R. W. Goosmann, M. Dovčiak, F. Muleri, N. Grosso, and V. Karas, "Modelling the X-ray polarimetric signatures of complex geometry: the case study of the 'changing look' active galactic nucleus NGC 1365," *Mon. Not. R. Astron. Soc.* **436**, 1615–1620 (2013).
39. H. P. Stahl, M. Postman, G. Mosier, W. S. Smith, C. Blaurock, K. Ha, and C. C. Stark, "AMTD: update of engineering specifications derived from science requirements for future UVOIR space telescopes," *Proc. SPIE* **9143**, 91438 (2014).
40. C. Marois, B. Macintosh, T. Barman, B. Zuckerman, I. Song, J. Patience, D. Lafrenière, and R. Doyon, "Direct imaging of multiple planets orbiting the star HR 8799," *Science* **322**, 1348–1352 (2008).
41. C. Marois, B. Zuckerman, Q. M. Konopacky, B. Macintosh, and T. Barman, "Images of a fourth planet orbiting HR 8799," *Nature* **468**, 1080–1083 (2010).
42. R. A. Brown and R. Soummer, "New completeness methods for estimating exoplanet discoveries by direct detection," *Astrophys. J.* **715**, 122–131 (2010).
43. C. C. Stark, A. Roberge, A. Mandell, and T. D. Robinson, "Maximizing the ExoEarth candidate yield from a future direct imaging mission," *Astrophys. J.* **795**, 122–142 (2014).
44. C. C. Stark, A. Roberge, A. Mandell, M. Clampin, S. D. Domagal-Goldman, M. W. McElwain, and K. R. Stapelfeldt, "Lower limits on aperture size for an ExoEarth detecting coronagraphic mission," *Astrophys. J.* **808**, 149–165 (2015).
45. Q. Kral, A. V. Krivov, D. Defrère, R. van Lieshout, A. Bonsor, J.-C. Augereau, P. Thébault, S. Ertel, J. Lebreton, and O. Absil, "Exozodiacal clouds: hot and warm dust around main sequence stars," *Astron. Rev.* **13**, 69–111 (2017).
46. M. Levine, D. Lisman, S. Shaklan, J. Kasting, W. Traub, J. Alexander, R. Angel, C. Blaurock, M. Brown, R. Brown, C. Burrows, M. Clampin, E. Cohen, D. Content, L. Dewell, P. Dumont, R. Egerman, H. Ferguson, V. Ford, J. Greene, O. Guyon, H. Hammel, S. Heap, T. Ho, S. Horner, S. Hunyadi, S. Irish, C. Jackson, J. Kasdin, A. Kissil, M. Krim, M. Kuchner, E. Kwack, C. Lillie, D. Lin, A. Liu, L. Marchen, M. Marley, V. Meadows, G. Mosier, P. Mouroulis, M. Noecker, R. Ohl, B. Oppenheimer, J. Pitman, S. Ridgway, E. Sabatke, S. Seager, M. Shao, A. Smith, R. Soummer, K. Stapelfeldt, D. Tenerell, J. Trauger, and R. Vanderbei, "Terrestrial Planet Finder Coronagraph (TPF-C) flight baseline concept," *arXiv e-prints* 0911.3200, 1–19 (2009).
47. G. B. Airy, "On the diffraction of an object-glass with circular aperture," *Trans. Cambridge Philos. Soc.* **5**, 283 (1835).
48. J. E. Harvey, K. L. Lewotsky, and A. Kotha, "Effects of surface scatter on the optical performance of x-ray synchrotron beam-line mirrors," *Appl. Opt.* **34**, 3024–3032 (1995).
49. J. D. Rhodes, R. J. Massey, J. Albert, N. Collins, R. S. Ellis, C. Heymans, J. P. Gardner, J.-P. Kneib, A. Koekemoer, A. Leauthaud, Y. Mellier, A. Refregier, J. E. Taylor, and L. V. Waerbeke, "The stability of the point-spread function of the Advanced Camera for Surveys on the Hubble Space Telescope and implications for weak gravitational lensing," *Astron. Astrophys. Suppl. Ser.* **172**, 203–218 (2007).

50. H. Hoekstra, "The effect of imperfect models of point spread function anisotropy on cosmic shear measurements," *Mon. Not. R. Astron. Soc.* **347**, 1337–1344 (2004).
51. G. M. Bernstein and M. Jarvis, "Shapes and shears, stars and smears: optimal measurements for weak lensing," *Astron. J.* **123**, 583–618 (2002).
52. K. R. Stapelfeldt, "Extrasolar planets and star formation: science opportunities for future ELTs," *Proc. Int. Astron. Union* **1**, 149–158 (2005).
53. H. Kawahara, T. Matsuo, M. Takami, Y. Fujii, T. Kotani, N. Murakami, M. Tamura, and O. Guyon, "Can ground-based telescopes detect the oxygen 1.27 μm absorption feature as a biomarker in exoplanets?" *Astrophys. J.* **758**, 1–11 (2012).
54. W. Cash, E. Schindhelm, J. Arenberg, A. Lo, R. Polidan, J. Kasdin, R. Vanderbei, S. Kilston, and C. Noecker, "External occulters for direct observation of exoplanets: an overview," *Proc. SPIE* **6687**, 668712 (2007).
55. R. J. Vanderbei, E. Cady, and N. J. Kasdin, "Optimal occulter design for finding extrasolar planets," *Astrophys. J.* **665**, 794–798 (2007).
56. M. W. Thomson, P. D. Lisman, R. Helms, P. Walkemeyer, A. Kissil, O. Polanco, and S.-C. Lee, "Starshade design for occulter based exoplanet missions," *Proc. SPIE* **7731**, 773153 (2010).
57. D. Mawet, N. Murakami, C. Delacroix, E. Serabyn, O. Absil, N. Baba, J. Baudrand, A. Boccaletti, R. Burruss, R. Chipman, P. Forsberg, S. Habraken, S. Hamaguchi, C. Hanot, A. Ise, M. Karlsson, B. Kern, J. Krist, A. Kuhnert, M. Levine, K. Liewer, S. McClain, S. McEldowney, B. Mennesson, D. Moody, H. Murakami, A. Niessner, J. Nishikawa, N. O'Brien, K. Oka, P. Park, P. Piron, L. Pueyo, P. Riaud, M. Sakamoto, M. Tamura, J. Trauger, D. Shemo, J. Surdej, N. Tabirian, W. Traub, J. Wallace, and K. Yokochi, "Taking the vector vortex coronagraph to the next level for ground- and space-based exoplanet imaging instruments: review of technology developments in the USA, Japan, and Europe," *Proc. SPIE* **8151**, 815114 (2011).
58. W. A. Traub, R. Belikov, O. Guyon, N. J. Kasdin, J. Krist, B. Macintosh, B. Mennesson, D. Savransky, M. Shao, E. Serabyn, and J. Trauger, "Science yield estimation for AFTA coronagraphs," *Proc. SPIE* **9143**, 91430N (2014).
59. P. Lawson, R. Belikov, W. Cash, M. Clampin, T. Glassman, O. Guyon, N. Kasdin, B. Kern, R. Lyon, and D. Mawet, "Survey of experimental results in high-contrast imaging for future exoplanet missions," *Proc. SPIE* **8864**, 88641F (2013).
60. S. Martin, D. Scharf, E. Cady, C. Liebe, and H. Tang, "Optical instrumentation for science and formation flying with a starshade observatory," *Proc. SPIE* **9605**, 960511 (2015).
61. D. P. Scharf, S. R. Martin, C. C. Liebe, Z. H. Rahman, C. R. Seubert, M. C. Noecker, and G. H. Purcell, "Precision formation flying at megameter separations for exoplanet characterization," *Acta Astronaut.* **123**, 420–434 (2016).
62. M. J. Kuchner and W. A. Traub, "A coronagraph with a band-limited mask for finding terrestrial planets," *Astrophys. J.* **570**, 900–908 (2002).
63. O. Guyon, E. A. Pluzhnik, R. Galicher, F. Martinache, S. T. Ridgway, and R. A. Woodruff, "Exoplanet imaging with a phase-induced amplitude apodization coronagraph. I. Principle," *Astrophys. J.* **622**, 744–758 (2005).
64. S. B. Shaklan, L. Marchen, E. Cady, W. Ames, P. D. Lisman, S. R. Martin, M. Thomson, and M. Regehr, "Error budgets for the Exoplanet Starshade (Exo-S) probe-class mission study," *Proc. SPIE* **9605**, 960514 (2015).
65. R. G. Lyon and M. Clampin, "Space telescope sensitivity and controls for exoplanet imaging," *Opt. Eng.* **51**, 011002 (2012).

66. S. B. Shaklan, L. Marchen, J. Krist, and M. Rud, "Stability error budget for an aggressive coronagraph on a 3.8 m telescope," *Proc. SPIE* **8151**, 815117 (2011).
67. M. T. Stahl, H. P. Stahl, and S. B. Shaklan, "Preliminary analysis of effect of random segment errors on coronagraph performance," *Proc. SPIE* **9605**, 96050P (2015).
68. G. Neugebauer, H. Habing, R. Van Duinen, H. Aumann, B. Baud, C. Beichman, D. Beintema, N. Boggess, P. Clegg, T. de Jong, J. P. Emerson, T. N. Gautier, F. C. Gillet, S. Harris, M. G. Hauser, J. R. Houck, R. E. Jennings, F. J. Low, P. L. Marsden, G. Miley, F. M. Olnon, S. R. Pottasch, E. Raimond, M. Rowan-Robinson, B. T. Soifer, R. G. Walker, P. R. Wesselius, and E. Young, "The infrared astronomical satellite (IRAS) mission," *Astrophys. J.* **278**, L1–L6 (1984).
69. M. Kessler, J. Steinz, M. Anderegg, J. Clavel, G. Drechsel, P. Estaria, J. Faelker, J. Riedinger, A. Robson, B. Taylor, and S. Ximénez de Ferrán, "The infrared space observatory (ISO) mission," *Astron. Astrophys.* **315**, L27–L31 (1996).
70. H. Murakami, H. Baba, P. Barthel, D. L. Clements, M. Cohen, Y. Doi, K. Enya, E. Figueredo, N. Fujishiro, H. Fujiwara, M. Fujiwara, P. Garcia-Lario, T. Goto, S. Hasegawa, Y. Hibi, T. Hirao, N. Hiromoto, S. S. Hong, K. Imai, M. Ishigaki, M. Ishiguro, D. Ishihara, Y. Ita, W.-S. Jeong, K. S. Jeong, H. Kaneda, H. Kataza, M. Kawada, T. Kawai, A. Kawamura, M. F. Kessler, D. Kester, T. Kii, D. C. Kim, W. Kim, H. Kobayashi, B. C. Koo, S. M. Kwon, H. M. Lee, R. Lorente, S. Makiuti, H. Matsuhara, T. Matsumoto, H. Matsuo, S. Matsuura, T. G. Müller, N. Murakami, H. Nagata, T. Nakagawa, T. Naoi, M. Narita, M. Noda, S. H. Oh, A. Ohnishi, Y. Ohyama, Y. Okada, H. Okuda, S. Oliver, T. Onaka, T. Ootsubo, S. Oyabu, S. Pak, Y.-S. Park, C. P. Pearson, M. Rowan-Robinson, T. Saito, I. Sakon, A. Salama, S. Sato, R. S. Savage, S. Serjeant, H. Shibai, M. Shirahata, J. Sohn, T. Suzuki, T. Takagi, H. Takahashi, T. Tanabé, T. T. Takeuchi, S. Takita, M. Thomson, K. Uemizu, M. Ueno, F. Usui, E. Verdugo, T. Wada, L. Wang, T. Watabe, H. Watarai, G. J. White, I. Yamamura, C. Yamauchi, and A. Yasuda, "The infrared astronomical mission AKARI," *Publ. Astron. Soc. Jpn.* **59**, S369–S376 (2007).
71. M. W. Werner, T. L. Roellig, F. J. Low, G. H. Rieke, M. Rieke, W. F. Hoffmann, E. Young, J. R. Houck, B. Brandl, G. G. Fazio, J. L. Hora, R. D. Gehrz, G. Helou, B. T. Soifer, J. Stauffer, J. Keene, P. Eisenhardt, D. Gallagher, T. N. Gautier, W. Irace, C. R. Lawrence, L. Simmons, J. E. V. Cleve, M. Jura, E. L. Wright, and D. P. Cruikshank, "The Spitzer Space Telescope mission," *Astrophys. J., Suppl. Ser.* **154**, 1–9 (2004).
72. M. Ferlet, N. Geis, J. Goicoechea, D. K. Griffin, A. M. Heras, K. Isaak, T. Nakagawa, T. Onaka, N. Rando, B. Swinyard, N. Takahashi, and S. Vives, "SPICA assessment study report," SRE-2009-6 (ESA, 2009).
73. G. Durand, M. Sauvage, A. Bonnet, L. Rodriguez, S. Ronayette, P. Chaniel, L. Scola, V. Révéret, H. Aussel, M. Carty, M. Durand, L. Durand, P. Tremblin, E. Pantin, M. Berthe, J. Martignac, F. Motte, M. Talvard, V. Minier, and P. Bultel, "TALC: a new deployable concept for a 20 m far-infrared space telescope," *Proc. SPIE* **9143**, 914311 (2014).
74. M. Sauvage, J. Amiaux, J. Austin, M. Bello, G. Bianucci, S. Chesné, O. Citterio, C. Collette, S. Correia, G. A. Durand, S. Molinari, G. Pareschi, Y. Penfornis, G. Sironi, G. Valsecchi, S. Verpoort, and U. Wittrock, "A development roadmap for critical technologies needed for TALC: a deployable 20 m annular space telescope," *Proc. SPIE* **9904**, 99041L (2016).
75. G. Durand, J. Amiaux, M. Sauvage, T. Martens, J. Austin, S. Chesne, C. Collette, J. Pareschi, Y. Penfornis, G. Valsecchi, and U. Wittrock, "TALC: a far-infrared 20 m space telescope and the ELICSIR consortium to reach TRL 3," *Proc. SPIE* **10562**, 105623R (2017).

76. G. L. Pilbratt, J. R. Riedinger, T. Passvogel, G. Crone, D. Doyle, U. Gageur, A. M. Heras, C. Jewell, L. Metcalfe, S. Ott, and M. Schmidt, "Herschel Space Observatory—an ESA facility for far-infrared and submillimetre astronomy," *Astron. Astrophys.* **518**, L1 (2010).
77. H. Dole, G. H. Rieke, G. Lagache, J.-L. Puget, A. Alonso-Herrero, L. Bai, M. Blaylock, E. Egami, C. W. Engelbracht, K. D. Gordon, D. C. Hines, D. M. Kelly, E. L. Floc'h, K. A. Misselt, J. E. Morrison, J. Muzerolle, C. Papovich, P. G. Pérez-González, M. J. Rieke, J. R. Rigby, G. Neugebauer, J. A. Stansberry, K. Y. L. Su, E. T. Young, C. A. Beichman, and P. L. Richards, "Confusion of extragalactic sources in the mid- and far-infrared: Spitzer and beyond," *Astrophys. J., Suppl. Ser.* **154**, 93–96 (2004).
78. H. Dole, G. Lagache, and J.-L. Puget, "Predictions for cosmological infrared surveys from space with the multiband imaging photometer for SIRTF," *Astrophys. J.* **585**, 617–629 (2003).
79. T. Onaka and T. Nakagawa, "SPICA: A 3.5 m space infrared telescope for mid- and far-infrared astronomy," *Adv. Space Res.* **36**, 1123–1127 (2005).
80. R. C. Kennicutt, D. Calzetti, G. Aniano, P. Appleton, L. Armus, P. Beirão, A. D. Bolatto, B. Brandl, A. Crocker, K. Croxall, D. A. Dale, J. D. Meyer, B. T. Draine, C. W. Engelbracht, M. Galametz, K. D. Gordon, B. Groves, C.-N. Hao, G. Helou, J. Hinz, L. K. Hunt, B. Johnson, J. Koda, O. Krause, A. K. Leroy, Y. Li, S. Meidt, E. Montiel, E. J. Murphy, N. Rahman, H.-W. Rix, H. Roussel, K. Sandstrom, M. Sauvage, E. Schinnerer, R. Skibba, J. D. T. Smith, S. Srinivasan, L. Vigroux, F. Walter, C. D. Wilson, M. Wolfire, and S. Zibetti, "KINGFISH-key insights on nearby galaxies: a far-infrared survey with Herschel: survey description and image atlas," *Publ. Astron. Soc. Pac.* **123**, 1347–1369 (2011).
81. T. Nakagawa, "The next-generation space infrared astronomy mission SPICA," *Proc. SPIE* **7731**, 77310O (2010).
82. M. Strojnik, "Stray-light issues for background-limited far-infrared telescope operation," *Opt. Eng.* **33**, 681–685 (1994).
83. W.-S. Jeong, H. Mok Lee, S. Pak, T. Nakagawa, S. Minn Kwon, C. P. Pearson, and G. J. White, "Far-infrared detection limits—I. Sky confusion due to galactic cirrus," *Mon. Not. R. Astron. Soc.* **357**, 535–547 (2005).
84. K. Yamada and T. Kitayama, "Infrared emission from intracluster dust grains and constraints on dust properties," *Publ. Astron. Soc. Jpn.* **57**, 611–619 (2005).
85. M.-A. Miville-Deschênes, G. Lagache, F. Boulanger, and J.-L. Puget, "Statistical properties of dust far-infrared emission," *Astron. Astrophys.* **469**, 595–605 (2007).
86. P. G. Martin, M.-A. Miville-Deschênes, A. Roy, J.-P. Bernard, S. Molinari, N. Billot, C. Brunt, L. Calzoletti, A. M. DiGiorgio, D. Elia, F. Faustini, G. Joncas, J. C. Mottram, P. Natoli, A. Noriega-Crespo, R. Paladini, J. F. Robitaille, F. Strafella, A. Traficante, and M. Veneziani, "Direct estimate of cirrus noise in Herschel Hi-GAL images," *Astron. Astrophys.* **518**, L105 (2010).
87. D. B. Doyle, "Current and future fabrication and testing challenges for European space optics," in *Classical Optics* (2014), paper OTh2B.1.
88. H. P. Stahl, "Advanced mirror technology development (AMTD): year five status," *Proc. SPIE* **10401**, 104010O (2017).
89. T. Döhring, "Polishers around the globe: an overview on the market of large astronomical mirrors," *Proc. SPIE* **9151**, 915110 (2014).
90. "2015 NASA technology roadmap," <https://www.nasa.gov/offices/oct/home/roadmaps/index.html>.
91. R. E. Parks, "Specifications: figure and finish are not enough," *Proc. SPIE* **7071**, 707109 (2008).

92. J. D. Hoyo, H. Choi, J. H. Burge, G.-H. Kim, and D. W. Kim, "Experimental power spectral density analysis for mid- to high-spatial frequency surface error control," *Appl. Opt.* **56**, 5258–5267 (2017).
93. A. M. Hvisc and J. H. Burge, "Structure function analysis of mirror fabrication and support errors," *Proc. SPIE* **6671**, 66710A (2007).
94. R. E. Parks, "Optical surface specification using the structure function," in *International Optical Design Conference and Optical Fabrication and Testing* (2010), paper OWE3.
95. M. J. Collon, M. Ackermann, R. Günther, A. Chatbi, G. Vacanti, M. Vervest, A. Yanson, M. W. Beijersbergen, M. Bavdaz, E. Wille, J. Haneveld, M. Olde Riekerink, A. Koelewijn, C. van Baren, P. Müller, M. Krumrey, V. Burwitz, G. Sironi, and M. Ghigo, "Making the ATHENA optics using silicon pore optics," *Proc. SPIE* **9144**, 91442G (2014).
96. M. J. Collon, G. Vacanti, R. Günther, A. Yanson, N. Barriere, B. Landgraf, M. Vervest, A. Chatbi, R. van der Hoeven, M. W. Beijersbergen, M. Bavdaz, E. Wille, B. Shortt, J. Haneveld, A. Koelewijn, C. van Baren, A. Eigenraam, P. Müller, M. Krumrey, V. Burwitz, G. Pareschi, P. Conconi, S. Massahi, F. E. Christensen, and G. Valsecchi, "Silicon pore optics development for ATHENA," *Proc. SPIE* **9603**, 96030K (2015).
97. K.-W. Chan, W. W. Zhang, M. V. Sharpe, J. R. Mazzarella, R. S. McClelland, M. P. Biskach, T. T. Saha, L. D. Kolos, and M.-L. Hong, "Preserving accurate figures in coating and bonding mirrors for lightweight x-ray telescopes," *Proc. SPIE* **9144**, 914413 (2014).
98. A. Leys, T. Hull, and T. Westerhoff, "Production of ELZM mirrors: performance coupled with attractive schedule, cost, and risk factors," *Proc. SPIE* **9911**, 99112P (2016).
99. G. W. Matthews, R. Egerman, S. P. Maffett, H. P. Stahl, R. Eng, and M. R. Effinger, "The development of stacked core technology for the fabrication of deep lightweight UV-quality space mirrors," *Proc. SPIE* **9143**, 91431U (2014).
100. T. Hobbs, M. Edwards, and A. Fox, "High volume ULE segment production," *Proc. SPIE* **9912**, 99123G (2016).
101. H. Martin, R. Allen, J. Burge, D. Kim, J. Kingsley, K. Law, R. Lutz, P. Strittmatter, P. Su, M. Tuell, S. C. West, and P. Zhou, "Production of 8.4 m segments for the Giant Magellan Telescope," *Proc. SPIE* **8450**, 84502D (2012).
102. E. Sein, Y. Toulemont, J. Breysse, P. Deny, D. de Chambure, T. Nakagawa, and M. Hirabayashi, "A new generation of large SiC telescopes for space applications," *Proc. SPIE* **5528**, 83–96 (2004).
103. K. Tsuno, H. Irikado, K. Hamada, O. Kazuhiko, J. Ishida, S. Suyama, Y. Itoh, N. Ebizuka, H. Eto, and Y. Dai, "Reaction-sintered silicon carbide: newly developed material for lightweight mirrors," *Proc. SPIE* **10568**, 105681F (2017).
104. R. Hu, W. Chen, Q. Li, S. Liu, P. Zhou, Z. Dong, and R. Kang, "Design optimization method for additive manufacturing of the primary mirror of a large-aperture space telescope," *J. Aerosp. Eng.* **30**, 04016093 (2017).
105. M. L. Jones, D. Walker, D. A. Naylor, I. T. Veenendaal, and B. G. Gom, "CFRP mirror technology for cryogenic space interferometry: review and progress to date," *Proc. SPIE* **9904**, 99046F (2016).
106. R. Hudec, V. Semencova, A. Inneman, M. Skulinova, L. Sveda, M. Míka, J. Sik, and M. Lorenc, "Space optics with silicon wafers and slumped glass," *Proc. SPIE* **10566**, 105660Q (2017).
107. M. J. Collon, G. Vacanti, R. Günther, A. Yanson, N. Barriere, B. Landgraf, M. Vervest, A. Chatbi, R. van der Hoeven, M. W. Beijersbergen, M. Bavdaz, E. Wille, B. Shortt, J. Haneveld, A. Koelewijn, C. van Baren, A. Eigenraam, P. Müller, M. Krumrey, V. Burwitz, G. Pareschi, P. Conconi, S. Massahi,

- F. E. Christensen, and G. Valsecchi, "Silicon pore optics for the ATHENA telescope," *Proc. SPIE* **9905**, 990528 (2016).
108. J. E. Koglin, H. An, N. Barrière, N. F. Brejnholt, F. E. Christensen, W. W. Craig, C. J. Hailey, A. C. Jakobsen, K. K. Madsen, K. Mori, M. Nynka, M. Fernandez-Perea, M. J. Pivovarov, A. Ptak, C. Sleator, D. Thornhill, J. K. Vogel, D. R. Wik, and W. W. Zhang, "First results from the ground calibration of the NuSTAR flight optics," *Proc. SPIE* **8147**, 814716 (2011).
109. A. Winter, E. Breunig, P. Friedrich, and L. Proserpio, "Progress on indirect glass slumping for future x-ray telescope optics," *Proc. SPIE* **9144**, 91441C (2014).
110. S. E. Kendrick and H. P. Stahl, "Large aperture space telescope mirror fabrication trades," *Proc. SPIE* **7010**, 701012 (2008).
111. S. Liu, R. Hu, Q. Li, P. Zhou, Z. Dong, and R. Kang, "Topology optimization-based lightweight primary mirror design of a large-aperture space telescope," *Appl. Opt.* **53**, 8318–8325 (2014).
112. "SCHOTT ZERODUR in astronomy," <http://www.us.schott.com/>.
113. J. Steeves, M. Laslandes, S. Pellegrino, D. Redding, S. C. Bradford, J. K. Wallace, and T. Barbee, "Design, fabrication and testing of active carbon shell mirrors for space telescope applications," *Proc. SPIE* **9151**, 915105 (2014).
114. D. A. Bath, D. Spain, E. Ness, S. Williams, and M. Bougoin, "Evaluation of segmented and brazed mirror assemblies," *Proc. SPIE* **5868**, 586805 (2005).
115. D. A. Bath, S. C. Williams, M. Bougoin, and G. J. Gardopee, "Fabrication and optical characterization of a segmented and brazed mirror assembly," *Proc. SPIE* **6666**, 66660L (2007).
116. M. Bougoin, "SiC challenging parts for GAIA," *Proc. SPIE* **10565**, 105652C (2017).
117. H. Kaneda, T. Nakagawa, T. Onaka, K. Enya, H. Kataza, S. Makiuti, H. Matsuhara, M. Miyamoto, H. Murakami, H. Saruwatari, H. Watarai, and Y. Y. Yui, "Development of lightweight SiC mirrors for the space infrared telescope for cosmology and astrophysics (SPICA) mission," *Proc. SPIE* **6666**, 666607 (2007).
118. B. Gallagher, M. Bergeland, B. Brown, D. Chaney, T. Copp, J. Lewis, B. Shogrin, K. Smith, J. Sokol, J. Hadaway, H. Glatzel, P. Johnson, A. Lee, D. Patriarca, I. Stevenson, J. Cluney, T. Parsonage, J. Calvert, B. Rodgers, A. McKay, S. Texter, L. Cohen, and L. Feinberg, "JWST mirror production status," *Proc. SPIE* **8146**, 814612 (2011).
119. T. B. Parsonage, "JWST beryllium telescope: material and substrate fabrication," *Proc. SPIE* **5494**, 39–49 (2004).
120. G. C. Cole, R. Garfield, T. Peters, W. Wolff, K. Johnson, R. Bernier, C. Kiiikka, T. Nassar, H. A. Wong, J. Kincade, T. Hull, B. Gallagher, D. Chaney, R. J. Brown, A. McKay, and L. M. Cohen, "An overview of optical fabrication of the JWST mirror segments at Tinsley," *Proc. SPIE* **6265**, 62650V (2006).
121. F.-J. Shiou and A. Asmare, "Parameters optimization on surface roughness improvement of Zerodur optical glass using an innovative rotary abrasive fluid multi-jet polishing process," *Precis. Eng.* **42**, 93–100 (2015).
122. C. J. Oh, A. E. Lowman, G. A. Smith, P. Su, R. Huang, T. Su, D. Kim, C. Zhao, P. Zhou, and J. H. Burge, "Fabrication and testing of 4.2 m off-axis aspheric primary mirror of Daniel K. Inouye Solar Telescope," *Proc. SPIE* **9912**, 99120O (2016).
123. D. W. Kim, C. J. Oh, P. Su, and J. H. Burge, "Advanced technology solar telescope 4.2 m off-axis primary mirror fabrication," in *Classical Optics* (2014), paper OTh2B.3.

124. P. Comley, P. Morantz, P. Shore, and X. Tonnellier, "Grinding metre scale mirror segments for the E-ELT ground based telescope," *CIRP Ann.* **60**, 379–382 (2011).
125. X. Tonnellier, P. Shore, P. Morantz, A. Baldwin, D. Walker, G. Yu, and R. Evans, "Sub-surface damage issues for effective fabrication of large optics," *Proc. SPIE* **7018**, 701810 (2008).
126. X. Xie, B. Yang, L. Zhou, C. Song, and H. Hu, "A large size ion beam figuring system for 1.2 m astronomical telescopes fabrication," *Proc. SPIE* **9912**, 99120E (2016).
127. M. Ghigo, G. Vecchi, S. Basso, O. Citterio, M. Civitani, E. Mattaini, G. Pareschi, and G. Sironi, "Ion figuring of large prototype mirror segments for the E-ELT," *Proc. SPIE* **9151**, 91510Q (2014).
128. E. R. R. Geyl and H. Leplan, "Advanced space optics development in freeform optics design, ceramic polishing, rapid and extreme freeform polishing," *Proc. SPIE* **10562**, 105623S (2017).
129. A. B. Shorey, W. Kordonski, and M. Tricard, "Magnetorheological finishing of large and lightweight optics," *Proc. SPIE* **5533**, 99–108 (2004).
130. J. H. Burge, D. W. Kim, and H. M. Martin, "Process optimization for polishing large aspheric mirrors," *Proc. SPIE* **9151**, 91512R (2014).
131. H. M. Martin, R. G. Allen, J. H. Burge, D. W. Kim, J. S. Kingsley, M. T. Tuell, S. C. West, C. Zhao, and T. Zobrist, "Fabrication and testing of the first 8.4-m off-axis segment for the Giant Magellan Telescope," *Proc. SPIE* **7739**, 77390A (2010).
132. H. M. Martin, J. R. P. Angel, G. Z. Angeli, J. H. Burge, W. Gressler, D. W. Kim, J. S. Kingsley, K. Law, M. Liang, D. Neill, J. Sebag, P. A. Strittmatter, M. T. Tuell, S. C. West, N. J. Woolf, and B. Xin, "Manufacture and final tests of the LSST monolithic primary/tertiary mirror," *Proc. SPIE* **9912**, 99120X (2016).
133. S. West, "Development and results for stressed-lap polishing of large telescope mirrors," in *Classical Optics* (2014), paper OTh2B.4.
134. D. W. Kim and J. H. Burge, "Rigid conformal polishing tool using non-linear visco-elastic effect," *Opt. Express* **18**, 2242–2257 (2010).
135. D. W. Kim, J. H. Burge, J. M. Davis, H. M. Martin, M. T. Tuell, L. R. Graves, and S. C. West, "New and improved technology for manufacture of GMT primary mirror segments," *Proc. SPIE* **9912**, 99120P (2016).
136. J. M. Davis, H. M. Martin, D. W. Kim, A. R. Loeff, K. L. Kenagy, R. W. Sisk, and J. R. Hagen, "Advances in diamond generating for 8.4 meter telescope mirrors," *Proc. SPIE* **9633**, 96330Y (2015).
137. C. L. Wyman and D. Korsch, "Aplanatic two-mirror telescopes: a systematic study. 1: Cassegrainian configuration," *Appl. Opt.* **13**, 2064–2066 (1974).
138. W. B. Wetherell and M. P. Rimmer, "General analysis of aplanatic Cassegrain, Gregorian, and Schwarzschild telescopes," *Appl. Opt.* **11**, 2817–2832 (1972).
139. C. L. Wyman and D. Korsch, "Systematic study of aplanatic two-mirror telescopes. 2: The Gregorian configuration," *Appl. Opt.* **13**, 2402–2404 (1974).
140. B. K. Smith, J. H. Burge, and H. M. Martin, "Fabrication of large convex mirrors," in *Fabrication and Testing of Aspheres* (1999), paper FT3.
141. A. P. Semenov, M. A. Abdulkadyrov, A. P. Patrikeev, V. E. Patrikeev, and V. V. Pridnya, "M1 and M2 mirror manufacturing for ARIES project: current status," *Proc. SPIE* **7739**, 773907 (2010).
142. B. K. Smith, J. H. Burge, and H. M. Martin, "Fabrication of large secondary mirrors for astronomical telescopes," *Proc. SPIE* **3134**, 51–61 (1997).
143. A. K. T. James and E. Harvey, "Scattering effects from residual optical fabrication errors," *Proc. SPIE* **2576**, 155–175 (1995).

144. J. H. Burge, W. Davison, H. M. Martin, and C. Zhao, "Development of surface metrology for the Giant Magellan Telescope primary mirror," *Proc. SPIE* **7018**, 701814 (2008).
145. T. L. Zobrist, J. H. Burge, and H. M. Martin, "Laser tracker surface measurements of the 8.4 m GMT primary mirror segment," *Proc. SPIE* **7426**, 742613 (2009).
146. M. A. Abdulkadyrov, V. E. Patrikeev, and A. P. Semenov, "Method of determining the ground aspheric surface profile of large astronomical mirrors," *J. Opt. Technol.* **81**, 714–718 (2014).
147. T. Su, W. H. Park, R. E. Parks, P. Su, and J. H. Burge, "Scanning long-wave optical test system: a new ground optical surface slope test system," *Proc. SPIE* **8126**, 812610 (2011).
148. T. Su, S. Wang, R. E. Parks, P. Su, and J. H. Burge, "Measuring rough optical surfaces using scanning long-wave optical test system. 1. Principle and implementation," *Appl. Opt.* **52**, 7117–7126 (2013).
149. C. Kiikka, D. R. Neal, J. Kincade, R. Bernier, T. Hull, D. Chaney, S. Farrer, J. Dixon, A. Causey, and S. Strohl, "The JWST infrared Scanning Shack Hartman System: a new in-process way to measure large mirrors during optical fabrication at Tinsley," *Proc. SPIE* **6265**, 626511 (2006).
150. P. Su, J. H. Burge, B. Cuerden, J. Sasian, and H. M. Martin, "Scanning pentaprism measurements of off-axis aspherics," *Proc. SPIE* **7426**, 74260Y (2008).
151. D. Castel, E. Sein, S. Lopez, T. Nakagawa, and M. Bougoin, "The 3.2 m all SiC telescope for SPICA," *Proc. SPIE* **8450**, 845013 (2012).
152. P. Su, R. E. Parks, L. Wang, R. P. Angel, and J. H. Burge, "Software configurable optical test system: a computerized reverse Hartmann test," *Appl. Opt.* **49**, 4404–4412 (2010).
153. R. Huang, P. Su, and J. H. Burge, "Deflectometry measurement of Daniel K. Inouye Solar Telescope primary mirror," *Proc. SPIE* **9575**, 957515 (2015).
154. P. Su, S. Wang, M. Khreishi, Y. Wang, T. Su, P. Zhou, R. E. Parks, K. Law, M. Rascon, T. Zobrist, H. Martin, and J. H. Burge, "SCOTS: a reverse Hartmann test with high dynamic range for Giant Magellan Telescope primary mirror segments," *Proc. SPIE* **8450**, 84500W (2012).
155. T. Su, A. Maldonado, P. Su, and J. H. Burge, "Instrument transfer function of slope measuring deflectometry systems," *Appl. Opt.* **54**, 2981–2990 (2015).
156. A. V. Maldonado, P. Su, and J. H. Burge, "Development of a portable deflectometry system for high spatial resolution surface measurements," *Appl. Opt.* **53**, 4023–4032 (2014).
157. I. Trumper, H. Choi, and D. W. Kim, "Instantaneous phase shifting deflectometry," *Opt. Express* **24**, 27993–28007 (2016).
158. S. Qian, H. Li, and P. Z. Takacs, "Penta-prism long trace profiler (PPLTP) for measurement of grazing incidence space optics," *Proc. SPIE* **2805**, 108–115 (1996).
159. J. L. Kirschman, E. E. Domning, W. R. McKinney, G. Y. Morrison, B. V. Smith, and V. V. Yashchuk, "Performance of the upgraded LTP-II at the ALS Optical Metrology Laboratory," *Proc. SPIE* **7077**, 707712 (2008).
160. X. Xu, Q. Huang, Z. Shen, and Z. Wang, "Improving the surface metrology accuracy of optical profilers by using multiple measurements," *Opt. Eng.* **55**, 104105 (2016).
161. S. Scheiding, M. Beier, U.-D. Zeitner, S. Risse, and A. Gebhardt, "Freeform mirror fabrication and metrology using a high performance test CGH and advanced alignment features," *Proc. SPIE* **8613**, 861315 (2013).

162. J. H. Burge, P. Su, and C. Zhao, "Optical metrology for very large convex aspheres," *Proc. SPIE* **7018**, 701818 (2008).
163. M. Dubin, P. Su, and J. H. Burge, "Fizeau interferometer with spherical reference and CGH correction for measuring large convex aspheres," *Proc. SPIE* **7426**, 74260S (2009).
164. A. Kulawiec, P. Murphy, and M. DeMarco, "Measurement of high-departure aspheres using subaperture stitching with the Variable Optical Null (VON)," *Proc. SPIE* **7655**, 765512 (2010).
165. S. Chen, S. Li, and G. Wang, "Subaperture test of wavefront error of large telescopes: error sources and stitching performance simulations," *Proc. SPIE* **9298**, 929817 (2014).
166. S. Chen, S. Xue, Y. Dai, and S. Li, "Subaperture stitching test of large steep convex spheres," *Opt. Express* **23**, 29047–29058 (2015).
167. M. A. Abdulkadyrov, "Methods of testing of large-size convex secondary mirrors with diameter up to 4 m," *Proc. SPIE* **8450**, 84504S (2012).
168. C. J. Oh, A. E. Lowman, M. Dubin, G. Smith, E. Frater, C. Zhao, and J. H. Burge, "Modern technologies of fabrication and testing of large convex secondary mirrors," *Proc. SPIE* **9912**, 99120R (2016).
169. H. Kaneda, T. Onaka, T. Nakagawa, K. Enya, H. Murakami, R. Yamashiro, T. Ezaki, Y. Numao, and Y. Sugiyama, "Cryogenic optical performance of the ASTRO-F SiC telescope," *Appl. Opt.* **44**, 6823–6832 (2005).
170. H. P. Stahl, "Rules for optical metrology," in *International Commission for Optics 22nd General Congress* (2011).
171. D. M. Chaney, J. B. Hadaway, J. Lewis, B. Gallagher, and B. Brown, "Cryogenic performance of the JWST primary mirror segment engineering development unit," *Proc. SPIE* **8150**, 815008 (2011).
172. J. B. Hadaway, D. M. Chaney, and L. B. Carey, "The optical metrology system for cryogenic testing of the JWST primary mirror segments," *Proc. SPIE* **8126**, 812611 (2011).
173. J. Kegley, M. Baker, J. Carpenter, R. Eng, H. Haight, W. Hogue, J. McCracken, K. Russell, R. Siler, and E. Wright, "Improved cryogenic testing capability at Marshall Space Flight Center's X-ray Cryogenic Facility," *Proc. SPIE* **6265**, 62654E (2006).
174. H. Kaneda, M. Naitoh, T. Imai, Y. Tange, K. Enya, H. Katayama, K. Maruyama, T. Nakagawa, T. Onaka, M. Sukanuma, R. Kano, Y. Kiriya, T. Mori, and A. Takahashi, "Cryogenic optical testing of an 800 mm lightweight C/SiC composite mirror mounted on a C/SiC optical bench," *Appl. Opt.* **49**, 3941–3948 (2010).
175. M. Kotani, T. Imai, H. Katayama, Y. Yui, Y. Tange, H. Kaneda, T. Nakagawa, and K. Enya, "Quality evaluation of spaceborne SiC mirrors (I): analytical examination of the effects on mirror accuracy by variation in the thermal expansion property of the mirror surface," *Appl. Opt.* **52**, 4797–4805 (2013).
176. M. Kotani, T. Imai, H. Katayama, Y. Yui, Y. Tange, H. Kaneda, T. Nakagawa, and K. Enya, "Quality evaluation of spaceborne SiC mirrors (II): evaluation technology for mirror accuracy using actual measurement data of samples cut out from a mirror surface," *Appl. Opt.* **52**, 6458–6466 (2013).
177. R. Eng, W. R. Arnold, M. A. Baker, R. M. Bevan, G. Burdick, M. R. Effinger, D. E. Gaddy, B. K. Goode, C. Hanson, W. D. Hogue, J. R. Kegley, C. Kirk, S. P. Maffett, G. W. Matthews, R. D. Siler, W. S. Smith, H. P. Stahl, J. M. Tucker, and E. R. Wright, "Cryogenic optical performance of a lightweighted mirror assembly for future space astronomical telescopes: correlating optical test results and thermal optical model," *Proc. SPIE* **8837**, 88370B (2013).

178. D. D. Allred, R. S. Turley, S. M. Thomas, S. G. Willett, M. J. Greenburg, and S. B. Perry, "Adding EUV reflectance to aluminum-coated mirrors for space-based observation," *Proc. SPIE* **10398**, 103980Y (2017).
179. R. C. Youngquist and M. A. Nurge, "Achieving cryogenic temperatures in deep space using a coating," *Opt. Lett.* **41**, 1086–1089 (2016).
180. K. Balasubramanian, J. Hennessy, N. Raouf, S. Nikzad, M. Ayala, S. Shaklan, P. Scowen, J. D. Hoyo, and M. Quijada, "Aluminum mirror coatings for UVOIR telescope optics including the far UV," *Proc. SPIE* **9602**, 96020I (2015).
181. C. S. Moore, J. Hennessy, E. Kersgaard, A. D. Jewell, S. Nikzad, and K. France, "Current progress in the characterization of atomic layer deposited AlF₃ for future astronomical ultraviolet mirror coatings," *Proc. SPIE* **9601**, 96010X (2015).
182. R. A. M. Keski-Kuha, J. I. Larruquert, J. S. Gum, and C. M. Fleetwood, "Optical coatings and materials for ultraviolet space applications," *Ultraviolet* **164**, 406 (1999).
183. J. J. Hennessy, K. Balasubramanian, C. S. Moore, A. D. Jewell, S. Nikzad, K. C. France, and M. A. Quijada, "Performance and prospects of far ultraviolet aluminum mirrors protected by atomic layer deposition," *J. Astron. Telesc. Instrum. Syst.* **2**, 041206 (2016).
184. J. Hennessy, C. S. Moore, K. Balasubramanian, A. D. Jewell, C. Carter, K. France, and S. Nikzad, "Atomic layer deposition and etching methods for far ultraviolet aluminum mirrors," *Proc. SPIE* **10401**, 1040119 (2017).
185. J. Hennessy, C. S. Moore, K. Balasubramanian, A. D. Jewell, K. France, and S. Nikzad, "Enhanced atomic layer etching of native aluminum oxide for ultraviolet optical applications," *J. Vac. Sci. Technol. A* **35**, 041512 (2017).
186. T. Döhring, A.-C. Probst, M. Stollenwerk, M. Wen, and L. Proserpio, "Development of low-stress Iridium coatings for astronomical x-ray mirrors," *Proc. SPIE* **9905**, 99056V (2016).
187. D. D. M. Ferreira, S. Massahi, F. E. Christensen, B. Shortt, M. Bavdaz, M. J. Collon, B. Landgraf, N. C. Gellert, J. Korman, P. Dalampiras, I. F. Rasmussen, I. Kamenidis, M. Krumrey, and S. Schreiber, "Design, development, and performance of x-ray mirror coatings for the ATHENA mission," *Proc. SPIE* **10399**, 1039918 (2017).
188. T. Schmid, K. Thompson, and J. Rolland, "Alignment induced aberration fields of next generation telescopes," *Proc. SPIE* **7068**, 70680E (2008).
189. T. Schmid, K. P. Thompson, and J. P. Rolland, "Misalignment-induced nodal aberration fields in two-mirror astronomical telescopes," *Appl. Opt.* **49**, D131–D144 (2010).
190. K. P. Thompson, K. Fuerschbach, T. Schmid, and J. P. Rolland, "Using nodal aberration theory to understand the aberrations of multiple unobscured three mirror anastigmatic (TMA) telescopes," *Proc. SPIE* **7433**, 74330B (2009).
191. Z. Gu, C. Yan, and Y. Wang, "Alignment of a three-mirror anastigmatic telescope using nodal aberration theory," *Opt. Express* **23**, 25182–25201 (2015).
192. D. C. Zimmerman, "Feasibility studies for the alignment of the thirty meter telescope," *Appl. Opt.* **49**, 3485–3498 (2010).
193. J. Sebag, W. Gressler, T. Schmid, J. P. Rolland, and K. P. Thompson, "LSST telescope alignment plan based on nodal aberration theory," *Publ. Astron. Soc. Pac.* **124**, 380–390 (2012).
194. R. Upton, M. Cho, and T. Rimmele, "Force-optimized alignment for optical control of the Advanced Technology Solar Telescope," *Appl. Opt.* **49**, G105–G113 (2010).

195. B. J. Bos, R. G. Ohl, and D. A. Kubalak, "Pupil alignment considerations for large deployable space telescopes," *Proc. SPIE* **8131**, 81310J (2011).
196. A. Dhabal, S. A. Rinehart, M. J. Rizzo, L. Mundy, H. Sampler, R. Juanola-Parramon, T. Veach, D. Fixsen, J. V. H. de Lorenzo, and R. F. Silverberg, "Optics alignment of a balloon-borne far-infrared interferometer BETTII," *J. Astron. Telesc. Instrum. Syst.* **3**, 024002 (2017).
197. D. S. Acton and J. S. Knight, "Multi-field alignment of the James Webb Space Telescope," *Proc. SPIE* **8442**, 84423C (2012).
198. A. C. Cheetham, P. G. Tuthill, A. Sivaramakrishnan, and J. P. Lloyd, "Fizeau interferometric cophasing of segmented mirrors," *Opt. Express* **20**, 29457–29471 (2012).
199. M. Deprez, B. Wattellier, C. Bellanger, L. Lombard, and J. Primot, "Phase measurement of a segmented wave front using PISon and TILt interferometry (PISTIL)," *Opt. Express* **26**, 5212–5224 (2018).
200. T. L. Whitman, C. Wells, J. B. Hadaway, J. S. Knight, and S. Lunt, "Alignment test results of the JWST Pathfinder Telescope mirrors in the cryogenic environment," *Proc. SPIE* **9904**, 990449 (2016).
201. J. B. Hadaway, C. Wells, G. Olczak, M. Waldman, T. Whitman, J. Cosentino, M. Connolly, D. Chaney, and R. Telfer, "Performance of the primary mirror center-of-curvature optical metrology system during cryogenic testing of the JWST Pathfinder telescope," *Proc. SPIE* **9904**, 99044E (2016).
202. "James Webb Space Telescope user documentation," <https://jwst-docs.stsci.edu/display/JTI/JWST+Wavefront+Sensing+and+Control>.
203. H. Choi, I. Trumper, M. Dubin, W. Zhao, and D. W. Kim, "Simultaneous multi-segmented mirror orientation test system using a digital aperture based on sheared Fourier analysis," *Opt. Express* **25**, 18152–18164 (2017).
204. K. Jackson, J. K. Wallace, and S. Pellegrino, "Co-phasing primary mirror segments of an optical space telescope using a long stroke Zernike WFS," *Proc. SPIE* **9904**, 99046D (2016).
205. N. J. Westergaard, K. K. Madsen, N. F. Brejnholt, J. E. Koglin, F. E. Christensen, M. J. Pivovarov, and J. K. Vogel, "NuSTAR on-ground calibration: I. Imaging quality," *Proc. SPIE* **8443**, 84431X (2012).
206. N. F. Brejnholt, F. E. Christensen, N. J. Westergaard, C. J. Hailey, J. E. Koglin, and W. W. Craig, "NuSTAR on-ground calibration: II. Effective area," *Proc. SPIE* **8443**, 844310 (2012).
207. Y. Ogasaka, K. Tamura, R. Shibata, A. Furuzawa, T. Miyazawa, K. Shimoda, Y. Fukaya, T. Iwahara, T. Nakamura, M. Naitou, Y. Kanou, N. Sasaki, D. Ueno, T. Okajima, E. Miyata, N. Tawa, K. Mukai, K. Ikegami, M. Aono, K. Uesugi, Y. Suzuki, S. Takeuchi, T. Futamura, R. Takahashi, M. Sakashita, C. Sakai, M. Nonoyama, N. Yamada, K. Onishi, T. Miyauchi, Y. Maeda, S. Okada, P. Serlemitsos, Y. Soong, K.-W. Chan, S. Rohrbach, F. Berendse, J. Tueller, H. Tsunemi, H. Kunieda, and K. Yamashita, "Characterization of a hard X-ray telescope at synchrotron facility SPring-8," *Jpn. J. Appl. Phys.* **47**, 5743–5754 (2008).
208. T. Miyazawa, Y. Ogasaka, T. Iwahara, Y. Kanou, Y. Makinae, S. Sasaya, T. Ohgi, K. Matsuda, M. Sakai, D. Niki, Y. Ishida, K. Yamane, A. Furuzawa, Y. Haba, H. Kunieda, K. Yamashita, K. Uesugi, Y. Suzuki, K. Tamura, Y. Maeda, M. Ishida, and T. Okajima, "Recent results from hard x-ray telescope characterization at SPring-8," *Proc. SPIE* **7437**, 74371P (2009).
209. R. Gracey, A. Bartoszyk, E. Cofie, B. Comber, G. Hartig, J. Howard, D. Sabatke, G. Wenzel, and R. Ohl, "Structural, thermal, and optical performance (STOP) modeling and results for the James Webb Space Telescope integrated science instrument module," *Proc. SPIE* **9911**, 99111A (2016).

210. S. R. Antonille, C. L. Miskey, R. G. Ohl, S. O. Rohrbach, D. L. Aronstein, A. E. Bartoszyk, C. W. Bowers, E. Cofie, N. R. Collins, B. J. Comber, W. L. Eichhorn, A. C. Glasse, R. Gracey, G. F. Hartig, J. M. Howard, D. M. Kelly, R. A. Kimble, J. R. Kirk, D. A. Kubalak, W. B. Landsman, D. J. Lindler, E. M. Malumuth, M. Maszkiewicz, M. J. Rieke, N. Rowlands, D. S. Sabatke, C. T. Smith, J. S. Smith, J. F. Sullivan, R. C. Telfer, M. Te Plate, M. B. Vila, G. D. Warner, D. Wright, R. H. Wright, J. Zhou, and T. P. Zielinski, "Optical testing and verification methods for the James Webb Space Telescope Integrated Science Instrument Module element," *Proc. SPIE* **9951**, 995105 (2016).
211. J. S. Knight, L. Feinberg, J. Howard, D. S. Acton, T. L. Whitman, and K. Smith, "Hartmann test for the James Webb Space Telescope," *Proc. SPIE* **9904**, 99040C (2016).
212. B. Saif, D. Chaney, W. S. Smith, P. Greenfield, W. Hack, J. Bluth, A. V. Otten, M. Bluth, J. Sanders, R. Keski-Kuha, L. Feinberg, M. North-Morris, and J. Millerd, "Nanometer level characterization of the James Webb Space Telescope optomechanical systems using high-speed interferometry," *Appl. Opt.* **54**, 4285–4298 (2015).
213. H. Kaneda, T. Nakagawa, K. Enya, Y. Tange, T. Imai, H. Katayama, M. Sukanuma, M. Naitoh, K. Maruyama, T. Onaka, Y. Kiriya, T. Mori, and A. Takahashi, "Optical testing activities for the SPICA telescope," *Proc. SPIE* **7731**, 77310V (2010).
214. H. Kaneda, T. Nakagawa, K. Enya, and T. Onaka, "Cryogenic optical testing of SiC mirrors for ASTRO-F and C/SiC composite mirrors for SPICA," *Proc. SPIE* **10568**, 105681H (2017).
215. H. Kaneda, M. Naitoh, T. Imai, H. Katayama, T. Onaka, T. Nakagawa, M. Kawada, M. Yamagishi, and T. Kokusho, "Experimental and numerical study of stitching interferometry for the optical testing of the SPICA telescope," *Proc. SPIE* **8442**, 84423T (2012).
216. P. Hallibert, "Active optics as enabling technology for future large missions: current developments for astronomy and Earth observation at ESA," *Proc. SPIE* **10401**, 1040118 (2017).
217. V. Costes, L. Perret, D. Laubier, J. M. Delvit, C. Imbert, L. Cadiergues, and C. Faure, "Active optics for next generation space telescopes," *Proc. SPIE* **10398**, 103980S (2017).
218. N. Devaney, A. Goncharov, M. Goy, C. Reinlein, and N. Lange, "Hypatia: a 4 m active space telescope concept and capabilities," *Proc. SPIE* **10562**, 1056235 (2017).
219. S. Kuiper, N. Doelman, E. Nieuwkoop, T. Overtoom, T. Russchenberg, M. van Riel, J. Wildschut, M. Baeten, J. Human, H. Spruit, S. Brinkers, and M. Maniscalco, "Electromagnetic deformable mirror development at TNO," *Proc. SPIE* **9912**, 991204 (2016).
220. P. Rausch, S. Verpoort, and U. Wittrock, "Unimorph deformable mirror for space telescopes: environmental testing," *Opt. Express* **24**, 1528–1542 (2016).
221. M. Goy, C. Reinlein, N. Devaney, A. Goncharov, R. Eberhardt, and A. Tünnermann, "Design study for an active metal mirror: sub-system of a correction chain for large UVOIR space telescopes," *Proc. SPIE* **10562**, 1056233 (2017).
222. R. Cousty, T. Antonini, M. Aubry, H. T. Krol, and A. Moreau, "Monomorph deformable mirrors: from ground-based facilities to space telescopes," *Proc. SPIE* **10562**, 1056231 (2017).
223. R. Angel, T. Kang, B. Cuerden, O. Guyon, and P. Stahl, "Active thermal figure control for the TOPS II primary mirror," *Proc. SPIE* **6693**, 669313 (2007).
224. R. Briguglio, C. Arcidiacono, M. Xompero, F. Lisi, A. Riccardi, R. Biasi, C. Patauner, D. Gallieni, P. Lazzarini, M. Tintori, F. d'Amato, M. Pucci,

- F. Duò, C. Vettore, and A. Z. Marchi, "The LATT way towards large active primaries for space telescopes," *Proc. SPIE* **9904**, 990410 (2016).
225. J. Steeves, K. Jackson, S. Pellegrino, D. Redding, J. K. Wallace, S. C. Bradford, and T. Barbee, "Multilayer active shell mirrors for space telescopes," *Proc. SPIE* **9912**, 991215 (2016).
226. R. S. Upton, "Presentation, analysis, and simulation of active alignment strategies for the James Webb Space Telescope," *Proc. SPIE* **7433**, 743302 (2009).
227. J. Mazoyer, L. A. Pueyo, C. A. Norman, M. N'Diaye, R. P. van der Marel, and R. Soummer, "Active compensation of aperture discontinuities for WFIRST-AFTA: analytical and numerical comparison of propagation methods and preliminary results with a WFIRST-AFTA-like pupil," *J. Astron. Telesc. Instrum. Syst.* **2**, 011008 (2015).
228. S. Sankar and J. Livas, "Testing and characterization of a prototype telescope for the evolved Laser Interferometer Space Antenna (eLISA)," *Proc. SPIE* **9904**, 99045A (2016).
229. E. Sakr and P. Bermel, "Angle-selective reflective filters for exclusion of background thermal emission," *Phys. Rev. Appl.* **7**, 044020 (2017).



Isaac Trumper is a Ph.D. student in the Large Optics Fabrication and Testing (LOFT) group at the College of Optical Sciences. His main research focuses on metrology development for large free-form and aspheric optics. He also has experience in optical design and software development. He received his B.S. in optics from the Institute of Optics at the University of Rochester in 2015.



Pascal Hallibert graduated from the Institut d'Optique Graduate School (Paris) in 1993, then worked as an optical engineer at SAGEM (France), TNO (Netherlands), and the Leiden Observatory (Netherlands). He is currently an optical systems engineer with the European Space Agency (ESA-ESTEC), providing optical support for projects such as Meteosat Third Generation and leading R&D studies in the fields of large aperture systems and active optics for space applications.



Jonathan W. Arenberg is the chief engineer for space science missions at Northrop Grumman Aerospace Systems. He has worked on the Chandra X-ray Observatory and the James Webb Space Telescope for over 12 years as chief engineer. His other work experience includes optical, space, and laser systems. He is a member of the U.S. National and International (ISO) committees charged with writing standards for laser and electro-optic systems. He holds a B.S. in physics and an M.S. and a Ph.D. in engineering, all from the University of California, Los Angeles. He has authored over 160 conference presentations, papers, book chapters, and professional short courses and a dozen European and U.S. patents in a wide range of technologies. He is the co-author of a forthcoming SPIE press book, *Systems Engineering for Astronomical Telescopes*. He belongs to the American Astronomical Society and is a fellow of SPIE.



Hideyo Kunieda is an executive advisor of Nagoya University, where he has been the professor at the Department of Physics, School of Science. He graduated from Nagoya University (Ph.D. in physics, 1982). He joined the faculty of the Department of Physics, Nagoya University, first as a research associate and later as an associate professor. He became professor at the Institute of Space and Astronautical Science in Kanagawa, Japan for 5.5 years and then moved back to Nagoya University. He has been involved in six Japanese x-ray missions (Hakucho, Tenma, Ginga, ASCA, Suzaku, and Hitomi) and one U.S. mission (Astro-1). His major contribution is in x-ray optics, especially high-throughput x-ray telescopes in collaboration with NASA Goddard Space Flight Center, where he stayed for two years in the 1980s. In the past eight years he has also been involved in the administration of Nagoya University as the dean of the School of Science and later as a vice president. He serves as a committee member of the International Astronomical Union Division IX and was the president of the Astronomical Society of Japan. Major interests in astronomy are active galactic nuclei that may harbor massive black holes. He has published 129 refereed papers (including 12 Nature papers).



Olivier Guyon is a physicist who uses his expertise in optics to design telescopes that investigate some of the most compelling issues in contemporary astronomy, particularly the search for Earth-like planets outside the solar system. Guyon invented an alternative coronagraphy method, phase-induced amplitude apodization (PIAA), which could reduce by nearly half the necessary instrument mirror diameter. This design significantly reduces the engineering and cost obstacles to deploying a planet-locating telescope in low-Earth orbit. In all aspects of his work, from theoretical calculations to laboratory fabrication, Guyon relentlessly tests and pushes boundaries to construct instruments that are key to one of the great scientific adventures of our time—searching the galaxy for other planets like our own.



H. Philip Stahl, senior optical physicist at NASA MSFC, is currently maturing mirror technologies and mission concepts for a large-aperture UVOIR telescope to replace Hubble. Previous assignments include developing JWST mirror technology. He is a leading authority in optical metrology, optical engineering, and phase-measuring interferometry. He is a fellow of OSA and a fellow of SPIE and was the 2014 SPIE president. He earned his Ph.D. in optical science at the University of Arizona, Optical Sciences Center in 1985.



Dae Wook Kim is an assistant professor of optical sciences and astronomy at the University of Arizona. He has been working in the optical engineering field for more than 10 years, mainly focusing on very large astronomical optics, such as the 25 m diameter Giant Magellan Telescope primary mirrors. His main research area covers the precision freeform optics fabrication and various metrology topics, such as interferometric test systems using computer generated holograms, direct curvature measurements,

and dynamic deflectometry systems. He is currently a chair/co-chair of the Optical Manufacturing and Testing conference (SPIE) and the Optical Fabrication and Testing conference (OSA). He is a senior member of OSA and SPIE and has been serving as an associate editor for the journal *Optics Express*.